

Towards exponentially-convergent simulations of extreme-mass-ratio inspirals: A time-domain solver for the scalar Teukolsky equation with singular source terms

Manas Vishal ^{1,2,*} Scott E. Field ^{1,2} Katherine Rink^{3,2,4} Sigal Gottlieb ^{1,2} and Gaurav Khanna^{5,3,2}

¹*Department of Mathematics, University of Massachusetts, Dartmouth, MA 02747, USA*

²*Center for Scientific Computing and Data Science Research, University of Massachusetts, Dartmouth, MA 02747, USA*

³*Department of Physics, University of Massachusetts, Dartmouth, MA 02747, USA*

⁴*Center for Gravitational Physics, University of Texas, Austin, TX 78712.*

⁵*Department of Physics and Center for Computational Research, University of Rhode Island, Kingston, RI 02881.*

(Dated: July 6, 2023)

Gravitational wave signals from extreme mass ratio inspirals are a key target for upcoming, space-based gravitational wave detectors. These systems are typically modeled as a distributionally-forced Teukolsky equation, where the smaller black hole is treated as a Dirac delta distribution (i.e., a point-particle). Time-domain solvers often use regularization approaches that approximate the Dirac distribution. Unfortunately, such approaches often introduce small length scales (e.g., when the approximation is by a narrow Gaussian) and are a source of systematic error, especially near the smaller black hole. We describe a multi-domain discontinuous Galerkin (DG) method for solving the distributionally-forced $s = 0$ Teukolsky equation that describes scalar fields evolving on a Kerr spacetime. To handle the Dirac delta, we expand the solution in spherical harmonics and recast the sourced Teukolsky equation as a first-order, one-dimensional symmetric hyperbolic system. This allows us to derive the method’s numerical flux to correctly account for the Dirac delta. As a result, our method achieves global spectral accuracy even at the source’s location. To connect the near field to future null infinity, we use the hyperboloidal layer method, allowing us to supply trivial outer boundary conditions and providing direct access to the far-field waveform. We document several numerical experiments where we test our method, including convergence tests against exact solutions, energy luminosities for circular orbits, the scheme’s superconvergence properties at future null infinity, and the late-time tail behavior of the scalar field. We also compare two systems that arise from different choices of the first-order reduction variables, finding that certain reasonable choices are numerically problematic in practice. The methods developed here may be beneficial when computing gravitational self-force effects, where the regularization procedure has been developed for the spherical harmonic modes and high accuracy is needed at the location of the Dirac delta.

I. INTRODUCTION

Black hole perturbation theory is a standard framework for studying a diverse range of gravitational phenomena, such as gravitational waves, quasi-normal modes, late-time Price tails, self-force effects, and linear stability of black hole solutions. The theory of such perturbations started with pioneering investigations by Regge and Wheeler [1–3] for Schwarzschild (nonspinning) black holes. The theory was later extended by Teukolsky to handle perturbations of the Kerr metric [4]. Small perturbations of a field with spin-weight s evolve on the Kerr geometry according to the Teukolsky master equation (1).

One important astrophysical application of black hole perturbation theory is to numerically simulate extreme mass ratio inspiral (EMRI) systems. An EMRI is comprised of small mass- q compact object orbiting a large mass- M black hole, where $q \ll M$. EMRI systems emit gravitational radiation at low frequencies and are a key target of the upcoming Laser Interferometer Space Antenna (LISA) observatory [5–7]. A standard method for studying EMRIs uses the perturbation theory of Kerr black holes in an approximation which treats the smaller

compact object as point-like and structureless. When a rotating black hole is perturbed by a small, compact object the Teukolsky equation features a source-term proportional to a Dirac delta distribution, $\delta(x)$, and possibly its derivatives.

Many numerical methods have been developed for the Teukolsky equation. Due to the separability of the Teukolsky equation in the frequency domain, frequency-domain solvers are one popular class of methods that have been extensively developed [8–12] and work especially well for sources that have a discrete frequency spectrum or approximately so like with adiabatically-driven inspiral.

Time-domain solvers [13–26], on the other hand, can generally handle a broader range of problems including high-eccentricity orbits and inspiral-merger-ringdown orbital regimes. Time-domain solvers are especially efficient when the source has a very broad or continuous Fourier spectrum. However, because the Teukolsky equation is not separable in the time-domain, most method development has focused on $2 + 1$ solvers: after expanding the field in angular modes $\exp(-im\phi)$ (the m -modes do separate) we are left with a differential equation with two spatial dimensions and time. The first $2 + 1$, time-domain solver was based on a Lax-Wendroff scheme [27]. Since then, various $2 + 1$ time-domain Teukolsky solvers have been developed based around pseudo-spectral [28] and weighted essentially non-oscillatory (WENO) [21] meth-

* vishalmanas28@gmail.com

ods. In particular, pseudo-spectral solvers are particularly well suited for smooth solutions while WENO methods are able to handle problems with sharp features such as those that arise in the computation of the Aretakis charge [29–31].

Despite the progress on time-domain methods for the source-free Teukolsky equation, particle-driven perturbations of the Kerr geometry remain challenging. To solve the distributionally-sourced Eq. (1), various regularized numerical approaches [16, 17, 32, 33] have been proposed. To our knowledge, all current treatments approximate the Dirac delta as a narrow Gaussian or discrete representations over an extended range of grid points [16, 17, 28]. In both cases, these methods introduce small length scales (e.g., when the approximation is a narrow Gaussian), which can be a source of systematic error and will impose smaller timestep restrictions when evolved with an explicit time-stepping method. We note that an alternative effective-source approach can also be applied to this problem by allowing for analytic modifications to the source term [34–36].

These problems have a clean solution for linear wave equations of one spatial variable. In previous work on the Regge-Wheeler-Zerilli and scalar wave equations, it was shown that a suitably modified multi-domain pseudo-spectral [37, 38] or discontinuous Galerkin (DG) [22, 39] method can exactly treat the Dirac delta distribution. Both methods (i) provide spectral accuracy even at its location, (ii) are especially well-suited for smooth solutions, which is the case away from the Dirac delta distribution. The main complication in applying the techniques of Ref. [22, 39] is that the Teukolsky equation is typically written in either $3+1$ or $2+1$ form. However, over the past few years multiple works have considered expanding the solution in (spin-weighted) spherical harmonics, leading to a coupled system of $1+1$ wave equations. To our knowledge, the benefits of this approach were first sketched out in [40–42], and the relevant equations written out in explicit form (in Boyer-Lindquist coordinates) to study source-free scalar [42] and gravitational [43] perturbations. And very recently this (source-free) system was also written in hyperboloidal coordinates and numerically solved with a symmetric integration method [44].

In this paper we describe a discontinuous Galerkin (DG) method [45–49] for solving the distributionally-sourced, $s=0$ Teukolsky equation describing scalar waves on Kerr. The main contribution of our work is to extend the numerical flux construction of Refs. [22, 39, 50] to the coupled $1+1$ system, Eq. (20). Our DG method discretizes this coupled system written in fully first-order form and achieves global spectral accuracy everywhere in the computational domain including at the particle’s location. Furthermore, at future null infinity (where the far-field signal is recorded) our method is super-convergent, thereby allowing for extremely accurate waveforms for a comparatively lower resolution numerical grid. As a by-product of our work, we also consider two systems that arise from different choices in the first-order reduc-

tion variables finding that certain choices are numerically problematic.

This paper is organized as follows. Section II derives the $1+1$ system in fully first-order form and discusses its hyperbolicity. The outer boundary, where we need to supply radiation outgoing boundary conditions and extract the far-field waveform, is handled using the method of hyperboloidal layers. The nodal discontinuous Galerkin method, and its generalization for incorporating Dirac delta distributions, are summarized in Sec. III. Section IV documents several experiments testing our method, including convergence tests against exact solutions in special cases where they are known, energy luminosities for circular orbits, and late-time tail behavior of the scalar field. Several appendices collect technical results and report on an alternative (and numerically problematic) formulation of the system.

II. EVOLUTION EQUATIONS

A. Teukolsky equation as a coupled 1+1D system

The Teukolsky master equation describes scalar, vector, and tensor field perturbations in the space-time of Kerr black holes [4]. In Boyer-Lindquist coordinates, this equation takes the form

$$\begin{aligned} & - \left[\frac{(r^2 + a^2)^2}{\Delta} - a^2 \sin^2 \theta \right] \partial_{tt} \Psi - \frac{4Mar}{\Delta} \partial_{t\phi} \Psi \\ & - 2s \left[r - \frac{M(r^2 - a^2)}{\Delta} + ia \cos \theta \right] \partial_t \Psi \\ & + \Delta^{-s} \partial_r (\Delta^{s+1} \partial_r \Psi) + \frac{1}{\sin \theta} \partial_\theta (\sin \theta \partial_\theta \Psi) + \\ & \left[\frac{1}{\sin^2 \theta} - \frac{a^2}{\Delta} \right] \partial_{\phi\phi} \Psi + 2s \left[\frac{a(r - M)}{\Delta} + \frac{i \cos \theta}{\sin^2 \theta} \right] \partial_\phi \Psi \\ & - (s^2 \cot^2 \theta - s) \Psi = -4\pi (r^2 + a^2 \cos^2 \theta) T, \end{aligned} \quad (1)$$

where M is the mass of the Kerr black hole, a its angular momentum per unit mass, $\Delta = r^2 - 2Mr + a^2$, s is the spin weight of the field, and T is a source term. The $s=0$ version of this equation describes scalar fields, and it is within this simpler setting that we will develop our methods.

Most time-domain numerical solvers do not directly discretize Eq. (1). Instead, due to the axisymmetry of the Kerr spacetime, a set of decoupled 2+1D equations can be derived by separating out the field’s azimuthal dependence. However, when the source term describes a point-particle, both the original 3+1D and the 2+1D systems are numerically challenging. For example, for the 3+1D system, if $T \propto \delta(r - r_p) \delta(\theta - \theta_p) \delta(\phi - \phi_p)$ then the solution is singular near (r_p, θ_p, ϕ_p) . Moreover, the methods of [39, 50], which exactly model the delta distribution as a modification to the numerical flux, are no longer directly applicable in 3+1D.

To overcome this issue, and to allow for exact treatment of the Dirac distribution, we follow Refs. [41–43] and derive a 1+1D coupled system of equations obeyed by the scalar field. We first expand the solution

$$\Psi(t, r, \theta, \phi) = \sum_{\ell=0}^{\infty} \sum_{m=-\ell}^{\ell} \Psi_{\ell m}(t, r) Y_{\ell m}(\theta, \phi), \quad (2)$$

in terms of the ordinary scalar spherical harmonics $Y_{\ell m}(\theta, \phi)$. We follow the same definition and conventions as Ref. [51] and, in particular, the harmonics are orthonormal when integrated over the sphere. Substituting Eq. (2) into Eq. (1) and using well-known properties of spherical harmonics we arrive at

$$\begin{aligned} & \sum_{\ell, m} \left[-(r^2 + a^2)^2 \ddot{\Psi}_{\ell m} - 4imMar \dot{\Psi}_{\ell m} + \Delta \partial_r (\Delta \partial_r \Psi_{\ell m}) \right. \\ & \left. + (a^2 m^2 - \ell(\ell + 1)\Delta) \Psi_{\ell m} + \Delta a^2 \sin^2 \theta \ddot{\Psi}_{\ell m} \right] Y_{\ell m} \\ & = -4\pi \Delta (r^2 + a^2 \cos^2 \theta) T. \end{aligned} \quad (3)$$

Here we use an over-dot to denote $\partial/\partial t$ differentiation. The term $\sin^2 \theta Y_{\ell m}$ is responsible for mode coupling, and we use relations from Ref. [52] to rewrite it as

$$\begin{aligned} \sin^2 \theta Y_{\ell m} &= c_{\ell m}^L Y_{Lm} \\ &= c_{\ell m}^{\ell-2} Y_{\ell-2, m} + c_{\ell m}^{\ell} Y_{\ell m} + c_{\ell m}^{\ell+2} Y_{\ell+2, m}, \end{aligned} \quad (4)$$

where, for brevity, we will use Einstein summation notation over the repeated “ L ” index. Appendix A provides the calculations needed to find these coupling coefficients. Multiplying by $\bar{Y}_{\ell' m'}$ and integrating over the sphere, we arrive at

$$\begin{aligned} & -(r^2 + a^2)^2 \ddot{\Psi}_{\ell m} - 4imMar \dot{\Psi}_{\ell m} + \Delta \partial_r (\Delta \partial_r \Psi_{\ell m}) \\ & + (a^2 m^2 - \ell(\ell + 1)\Delta) \Psi_{\ell m} + \Delta a^2 c_{Lm}^{\ell} \ddot{\Psi}_{Lm} = \hat{g}_{\ell m}(t, r), \end{aligned} \quad (5)$$

where the overline denotes complex conjugation, $c_{Lm}^{\ell} \ddot{\Psi}_{Lm} = c_{(\ell-2)m}^{\ell} \ddot{\Psi}_{(\ell-2)m} + c_{\ell m}^{\ell} \ddot{\Psi}_{\ell m} + c_{(\ell+2)m}^{\ell} \ddot{\Psi}_{(\ell+2)m}$, and

$$\hat{g}_{\ell m}(t, r) = -4\pi \Delta \int (r^2 + a^2 \cos^2 \theta) \bar{Y}_{\ell m} T d\Omega, \quad (6)$$

is the source term.

We now factor out the large- r behavior of $\Psi_{\ell m}$,

$$\Psi_{\ell m} = \frac{\psi_{\ell m}}{\sqrt{r^2 + a^2}}, \quad (7)$$

and to map out the background spacetime, we introduce the tortoise coordinate, r_* , defined by

$$dr_* = \frac{r^2 + a^2}{\Delta} dr. \quad (8)$$

In terms of $\psi_{\ell m}$ and r_* , Eq. (5) becomes

$$\begin{aligned} f - \ddot{\psi}_{\ell m} + \partial_{r_*} \partial_{r_*} \psi_{\ell m} + \frac{\Delta a^2}{(r^2 + a^2)^2} c_{Lm}^{\ell} \ddot{\psi}_{Lm} \\ - \frac{4imMar}{(r^2 + a^2)^2} \dot{\psi}_{\ell m} + V_{\ell m}(r) \psi_{\ell m} = g_{\ell m}(t, r), \end{aligned} \quad (9)$$

where $\psi = \psi(t, r_*)$, $g_{\ell m} = \hat{g}_{\ell m}/(r^2 + a^2)^{\frac{3}{2}}$ and,

$$\begin{aligned} V_{\ell m}(r) = & \left[\frac{3r^2 \Delta^2}{(r^2 + a^2)^4} - \frac{2r \Delta (r - M)}{(r^2 + a^2)^3} \right. \\ & \left. - \frac{\Delta^2}{(r^2 + a^2)^3} + \frac{a^2 m^2}{(r^2 + a^2)^2} - \frac{\ell(\ell + 1)\Delta}{(r^2 + a^2)^2} \right]. \end{aligned} \quad (10)$$

The resulting differential equation’s principle part is particularly simple [53] and reduces to the ordinary wave operator when $a = 0$. Eq. (9) is the one we numerically solve after carrying out a reduction to fully first-order form and transforming it to hyperboloidal coordinates; refer to Sec. IIC and Sec. IID.

B. Distributional source term due to a scalar-charged particle in circular orbit

In this subsection, we provide expressions for the sourcing functions, $g_{\ell m}(t)$, that arise from projecting the scalar charge density, T , onto the spherical harmonics. Following the standard setup, we assume our problem arises from a small “particle” of mass q orbiting a large-mass M Kerr blackhole, where the mass ratio satisfies $q/M \ll 1$. Ignoring radiation-reaction effects and specializing to circular and equatorial geodesic orbits, the particle’s scalar charge density is given by [54]

$$T = \frac{q}{r_p^2 u^t} \delta(r - r_p) \delta(\theta - \theta_p) \delta(\phi - \phi_p(t)), \quad (11)$$

where the constant r_p denotes the particle’s radial position, $\theta_p = \pi/2$ denotes the particle’s polar angle, u^t is the t -component of the particle’s four-velocity, and $\phi_p(t)$ is the particle’s angular location. Expressions for

$$u^t = g^{t\phi} \mathcal{L} - g^{tt} \mathcal{E}, \quad \phi_p(t) = \frac{v^3}{M(1 + \tilde{a}v^3)} t, \quad (12)$$

are readily given in, for example, Refs. [54, 55]. Here $v = \sqrt{M/r_p}$, $\tilde{a} = a/M$, and

$$\mathcal{E} = \frac{1 - 2v^2 + \tilde{a}v^3}{\sqrt{1 - 3v^2 + 2\tilde{a}v^3}}, \quad \mathcal{L} = r_p v \frac{1 - 2\tilde{a}v^3 + \tilde{a}^2 v^4}{\sqrt{1 - 3v^2 + 2\tilde{a}v^3}}, \quad (13)$$

are, respectively, the particle’s energy and angular momentum. The background Kerr metric is denoted by $g_{\mu\nu}$.

With these preliminaries in place, for motion in the orbital plane and viewing $g_{\ell m}$ as a function of r_* , we now straightforwardly compute

$$g_{\ell m}(t, r_*) = \frac{-4\pi q}{u^t (r_p^2 + a^2)^{1/2}} \bar{Y}_{\ell m} \left(\frac{\pi}{2}, \phi_p(t) \right) \delta(r_* - r_{*,p}), \quad (14)$$

where we have used $\delta(r - r_p) = [(r_p^2 + a^2)/\Delta_p] \delta(r_* - r_{*,p})$ to transform the Dirac distribution into r_* coordinates.

C. Reduction to first-order form

For wave-like problems, the discontinuous Galerkin method we will introduce in Sec. III is most readily applicable to systems in fully first-order form. Towards this end, we introduce two new variables,

$$\pi_{\ell m} = -\frac{\partial\psi_{\ell m}}{\partial t}, \quad \phi_{\ell m} = \frac{\partial\psi_{\ell m}}{\partial r_*}. \quad (15)$$

The following first-order system corresponds to the original second-order wave equation (9):

$$\dot{\psi}_{\ell m} = -\pi_{\ell m}, \quad (16a)$$

$$\dot{\pi}_{\ell m} - f c_{Lm}^{\ell} \dot{\pi}_{Lm} = -\partial_{r_*} \phi_{\ell m} - \mu \pi_{\ell m} - V_{\ell m}(r) \psi_{\ell m} + g_{\ell m}(t, r), \quad (16b)$$

$$\dot{\phi}_{\ell m} = -\partial_{r_*} \pi_{\ell m}. \quad (16c)$$

In these expressions and below we will use

$$f = \frac{\Delta a^2}{(r^2 + a^2)^2}, \quad \mu = \frac{4imMar}{(r^2 + a^2)^2}, \quad (17)$$

for convenience. If $\psi_{\ell m}$ solves the first-order system (16) it also solves the original second-order equation (9) provided the constraint $\phi_{\ell m} = \partial_{r_*} \psi_{\ell m}$. We note that alternative reduction variables could also be used. One such seemingly-reasonable choice ($\pi_{\ell m} = -\partial_{\tau} \psi_{\ell m}$ and $\phi_{\ell m} = \partial_{\rho} \psi_{\ell m}$) is considered in App. D, and in Sec. IV we demonstrate that this choice appears to be numerically problematic. While we have not shown this system to be theoretically problematic, under certain conditions our preferred choice of reduction variables (15) leads to a symmetric hyperbolic (and hence well-posed) initial-boundary-value problem.

D. Hyperboloidal layers

The numerical simulation of wave phenomena on an open domain requires the specification of radiation boundary conditions and, in the case of gravitational-wave simulations, access to the waves that reach future null infinity. We use the method of hyperboloidal layers [19, 56] to solve both issues at the outermost physical boundary. We first introduce hyperboloidal coordinates, (ρ, τ) , defined by

$$r_* = \frac{\rho}{\Omega(\rho)}, \quad \tau = t - h(r_*), \quad (18)$$

that are related to the original (r_*, t) coordinates through specification of the functions,

$$\Omega = 1 - \left(\frac{\rho - R}{s - R}\right)^P \Theta(\rho - R), \quad h = \frac{\rho}{\Omega} - \rho, \quad (19)$$

where R , s , and P are to-be-set parameters and Θ is the Heaviside step function. To the left of the timelike surface defined by $\rho = R$, the coordinates are the original (r_*, t)

ones. To the right of $\rho = R$, the coordinates smoothly connect the computational domain to future null infinity, which is defined by $\rho = s$. The width of the hyperboloidal layer is given by $s - R$. We will choose the location of interface R such that (i) the source term is always located to the left of the interface and (ii) for our multi-domain method, we collocate the start of the layer at a subdomain interface. A sufficiently smooth coordinate transformation can be achieved by setting the value of P , typically taken to be a positive integer [57]. The value of P , in turn, can impact the numerical scheme's order of convergence. In Fig. 2 we systematically vary P to find values that maintain our DG method's superconvergence property. Besides this one numerical experiment we use $P = 4$ throughout this paper.

In hyperboloidal coordinates, Eq. (16) becomes ¹

$$\dot{\psi}_{\ell m} = -\pi_{\ell m}, \quad (20a)$$

$$\dot{\pi}_{\ell m} - f c_{Lm}^{\ell} \dot{\pi}_{Lm} - H \dot{\phi}_{\ell m} = -(1 - H) \phi'_{\ell m} - \mu \pi_{\ell m} - V_{\ell m}(r) \psi_{\ell m} + g_{\ell m}(t, r), \quad (20b)$$

$$\dot{\phi}_{\ell m} - H \dot{\pi}_{\ell m} = -(1 - H) \pi'_{\ell m}, \quad (20c)$$

where we now use an over-dot to denote $\partial/\partial\tau$ differentiation, a prime for differentiation by $\partial/\partial\rho$, and we note that $\partial/\partial\tau = \partial/\partial t$. Here $H = \partial h/\partial r_* = 1 - \partial\rho/\partial r_*$ and, for later use, we note that

$$H = 1 - \frac{\Omega^2}{\Omega - \rho\Omega'}, \quad H' = \frac{dH}{d\rho} = -\omega', \quad (21)$$

where $\omega = \Omega^2/(\Omega - \rho\Omega')$. To the left of the layer, where $\rho < R$, we have $H = 0$ and so both Eq. (16) and Eq. (20) are identical. One important fact of this coordinate transformation, which we will use later on, is that the outgoing characteristics obey $\tau - \rho = t - r_*$. While the coordinate transformation is singular at $\rho = s$, the coefficients of each term in Eq. (20) are finite. This can be seen by noting that as $\rho \rightarrow s$ we have $(1 - H) \sim \Omega^2 \sim r_*^{-2} \sim r^{-2}$ [19, 56].

E. Truncating to a finite number of modes

To achieve a finite number of equations, the expansion Eq. (2) must be truncated to a finite value ℓ_{\max} . Let Ψ_{full} be the infinite series (2) and $\Psi_{\ell_{\max}}$ the truncated expansion. Then the angular truncation error for $a = 0$ (no mode mixing) is

$$\Psi_{\text{full}} - \Psi_{\ell_{\max}} = \sum_{\ell=\ell_{\max}+1}^{\infty} \sum_{m=-\ell}^{\ell} \Psi_{\ell m}(t, r) Y_{\ell m}(\theta, \phi). \quad (22)$$

¹ When enacting this coordinate transformation we do not let $\pi_{\ell m}$ and $\phi_{\ell m}$ transform. If we did, the resulting system would be the problematic one considered in App. D.

Integrating the residual over the sphere, we arrive at

$$\delta\Psi = \sum_{\ell=\ell_{\max}+1}^{\infty} \sum_{m=-\ell}^{\ell} |\Psi_{\ell m}(t, r)|^2,$$

where $|\cdot|$ is the complex modulus. Due to the expected decay of the coefficients $\Psi_{\ell m}(t, r)$, we can estimate the angular approximation error as $\delta\Psi \approx \sum_{m=-\ell_{\max}}^{\ell_{\max}} |\Psi_{\ell m}(t, r)|^2$, which can be monitored throughout the simulation. For $a \neq 0$, ℓ modes will mix, but we can nonetheless use this estimation as a useful guide. While the angular approximation might seem like a limitation to our method, we point out that this error shows up under a different guise in any numerical scheme. For example, traditional 2+1 solvers that discretize the ∂_{θ} operator effectively set a resolution for the maximum resolvable ℓ -mode. In all cases, one can estimate the error by increasing the angular grid resolution (for traditional 2+1 solvers) or ℓ_{\max} (our angular resolution error).

F. Matrix form

We now turn to writing Eq. (20) in matrix form, which will prove useful later on. Let ℓ_{\max} be the largest value of ℓ we will consider in the computation, that is we make an approximation $\psi_{\ell m} = 0$ for $\ell > \ell_{\max}$. Noting that (i) the equation for odd and even ℓ modes decouple and (ii) each m mode decouples, let us define a solution vector for the even- ℓ mode, $U_{\ell_{\max}m}^{\text{even}} = [\vec{\pi}_{\ell_{\max}m}^{\text{even}}, \vec{\phi}_{\ell_{\max}m}^{\text{even}}]^T$, where

$$\vec{\pi}_{\ell_{\max}m}^{\text{even}} = [\pi_{\ell_{\min}m}^{\text{even}}, \pi_{(\ell_{\min}+2)m}^{\text{even}}, \dots, \pi_{\ell_{\max}m}^{\text{even}}]^T, \quad (23)$$

$$\vec{\phi}_{\ell_{\max}m}^{\text{even}} = [\phi_{\ell_{\min}m}^{\text{even}}, \phi_{(\ell_{\min}+2)m}^{\text{even}}, \dots, \phi_{\ell_{\max}m}^{\text{even}}]^T. \quad (24)$$

We have introduced ℓ_{\min} for the smallest value of ℓ given m and the even/odd mode type. For example, if $m = 0$ we have $\ell_{\min} = 0$ (1) for the even (odd) modes, while if $m = 2$, we have $\ell_{\min} = 2$ (3) for the even (odd) modes. A similar set of notation is equally applicable to the odd- ℓ modes, leading to the system vector $U_{\ell_{\max}m}^{\text{odd}}$.

The coupled system of equations (20)(b,c) take the form,

$$E\dot{U} + \hat{A}U' + \hat{B}(U) + \hat{V}(\psi) = \hat{G}(t)\delta(r_* - r_{*,p}), \quad (25)$$

where the components of E , \hat{A} , \hat{B} , and \hat{V} can be read off from Eq. (20). The vector $\hat{G}(t)$ contains the coefficients of the distributional source term shown in Eq. (14). In this expression, we have dropped the m , ℓ_{\max} , and {odd, even} labels from both the matrices and solution vector for clarity. The remaining set of equations, $\dot{\psi}_{\ell m} = -\pi_{\ell m}$, are trivially evolved along with the Eq. (25). Clearly the size of these matrices change with ℓ_{\max} and m . For example, choosing (type, ℓ_{\max} , m) = (even, 8, 0) will result in a 10-by-10 system, while (type, ℓ_{\max} , m) = (even, 8, 4) will

yield a 6-by-6 system. Inverting E , Eq. (25) becomes

$$\dot{U} + AU' + B(U) + V(\psi) = G(t)\delta(r_* - r_{*,p}), \quad (26)$$

where we have defined $A = E^{-1}\hat{A}$, $B = E^{-1}\hat{B}$, $V = E^{-1}\hat{V}$, and $G = E^{-1}\hat{G}$. We summarize the discretization of system, Eq. (26) in Sec. III.

For concreteness, consider the even ℓ -mode sector with $m = 0$ and $\ell_{\max} = 2$; App. B considers the most general system. Then we have $U = [\pi_{00}, \pi_{20}, \phi_{00}, \phi_{20}]^T$, and

$$E = \begin{bmatrix} 1 - fc_{00}^0 & -fc_{20}^0 & -H & 0 \\ -fc_{00}^2 & 1 - fc_{20}^2 & 0 & -H \\ -H & 0 & 1 & 0 \\ 0 & -H & 0 & 1 \end{bmatrix}, \quad (27)$$

and

$$\hat{A} = \begin{bmatrix} 0 & 0 & (1-H) & 0 \\ 0 & 0 & 0 & (1-H) \\ (1-H) & 0 & 0 & 0 \\ 0 & (1-H) & 0 & 0 \end{bmatrix}, \quad (28)$$

with

$$\hat{V} = [V_0\psi_{00}, V_2\psi_{20}, 0, 0]^T, \quad (29)$$

$$\hat{B} = [\mu\pi_{00}, \mu\pi_{20}, 0, 0]^T. \quad (30)$$

The components of the source vector are given by

$$\hat{G} = \frac{-4\pi q}{u^t (r_p^2 + a^2)^{1/2}} [\overline{Y}_{00}, \overline{Y}_{20}, 0, 0]^T, \quad (31)$$

where the spherical harmonics are evaluated at $\theta = \pi/2$ and $\phi = \phi_p(t)$.

G. System hyperbolicity

We now consider the system's hyperbolicity, which has important consequences for the numerics and is directly used in the construction of the numerical flux. As shown in App. B, when $a = 0$ the system (25) is symmetric hyperbolic and we conjecture this to be true for $a \neq 0$ too. If we had instead used $\pi_{\ell m} = -\partial_{\tau}\psi_{\ell m}$ and $\phi_{\ell m} = \partial_{\rho}\psi_{\ell m}$ as our first-order reduction variables, the resulting system (D3) is not symmetric hyperbolic even when $a = 0$. In principle this isn't necessarily an issue, but we have found through extensive experimentation that our numerical scheme when applied to this alternative system shows a catastrophic loss of accuracy near $\rho = s$ (cf. Fig. 3 and Table II). This alternative system and its hyperbolicity are discussed in App. D.

To study the system's wave structure, we consider the principle part of Eq. (26),

$$\dot{U} + AU' + \dots = 0, \quad (32)$$

and diagonalize the matrix A

$$A(\rho) = T(\rho)\Lambda(\rho)T^{-1}(\rho). \quad (33)$$

Let us assume U is of length L , then T is an L -by- L matrix whose i^{th} column is the right eigenvector of A corresponding to the eigenvalue $\lambda_i(\rho)$. The eigenvalues are real and correspond to the entries of the diagonal matrix $\Lambda = \text{diag}(\lambda_1, \lambda_2, \dots, \lambda_L)$. Furthermore, the eigenvalues satisfy $-1 \leq \lambda_i \leq 1$. Noting that L is always even, half of the eigenvalues are 1 and half of the eigenvalues are non-positive at $\rho < s$ and become exactly 0 at $\rho = s$.

Assuming “frozen” matrix coefficients and letting $C = T^{-1}U$, the principle part of the system can be written as

$$\dot{C} + \Lambda C' = 0. \quad (34)$$

Then, like the simple advection equation, $\lambda_i > 0$ corresponds to outgoing waves moving at a speed λ_i while $\lambda_i < 0$ corresponds to incoming waves moving at a speed $|\lambda_i|$. For later use in Sec. III C, we split the diagonal matrix as $\Lambda = \Lambda^+ + \Lambda^-$, where Λ^+ (Λ^-) contains only positive (negative) eigenvalues. We then define the projection matrix P^+ as Λ^+ with non-zero entries replaced by 1. Similarly, let P^- be Λ^- with non-zero entries replaced by 1. With this new notation, the non-zero components of P^+C and P^-C are, respectively, the right-moving and left-moving waves. These projection operators are used in the construction of the numerical flux given Sec. III C.

H. Boundary conditions

Due to the hyperboloidal coordinate transformation, the wave speeds of system, Eq. (20) at the right physical boundary $\rho = s$ are either 1 or 0. This means $\rho = s$ is an outflow boundary and hence no boundary conditions are needed. For the left boundary, we note that the system includes a mixture of incoming and outgoing characteristics and, furthermore, the potential is non-zero at the horizon when $m \neq 0$ and $a \neq 0$. We impose Sommerfeld boundary conditions setting the incoming characteristics to zero. This will lead to spurious reflection that can be mitigated by placing the left boundary at a sufficiently negative value of ρ such that the left boundary is causally disconnected in the region of the computational domain that we care about. We note that this boundary issue can be solved by enacting so-called azimuthal transformations [58, 59], which we do not consider here.

I. Energy flux

One important application of the distributionally-sourced scalar wave equation is computing energy luminosities. Here we provide a formula for this quantity in terms of our system variables.

The radiative energy flux across an arbitrarily large ($r \rightarrow \infty$) spherical surface will form the basis of some of our numerical experiments. The energy flux is given

by [54],

$$\dot{E} = \frac{dE}{dt} = -\Delta \oint T_{tr} d\Omega, \quad (35)$$

where the stress-energy tensor

$$T_{\alpha\beta} = \frac{1}{4\pi} \left(\partial_\alpha \Psi \partial_\beta \Psi - \frac{1}{2} g_{\alpha\beta} \partial^\mu \Psi \partial_\mu \Psi \right), \quad (36)$$

is determined from derivatives of the scalar field. Noting that the scalar field is real, we first write $T_{tr} = -\Psi_{,t} \overline{\Psi_{,r}} / (4\pi)$, then substitute

$$\Psi(t, r, \theta, \phi) = \frac{1}{\sqrt{r^2 + a^2}} \sum_{\ell=0}^{\infty} \sum_{m=-\ell}^{\ell} \psi_{\ell m}(t, r) Y_{\ell m}(\theta, \phi), \quad (37)$$

to arrive at the individual multipole contributions to the total energy flux through the sphere at infinity,

$$\dot{E} = -\frac{1}{4\pi} \sum_{\ell, m} \psi_{,t}^{\ell m} \overline{\psi_{,r}^{\ell m}} = \frac{1}{4\pi} \sum_{\ell, m} |\psi_{,t}^{\ell m}|^2 = \frac{1}{4\pi} \sum_{\ell, m} |\pi^{\ell m}|^2, \quad (38)$$

where we made use of the fact that in the asymptotic limit ($r \rightarrow \infty$) the outgoing radiation condition implies $\psi_{,t} = -\psi_{,r}$. We will often directly compare the multipole contributions $\dot{E}_{\ell m} = |\pi^{\ell m}|^2 / (4\pi)$.

III. THE DISCONTINUOUS GALERKIN SCHEME

Discontinuous Galerkin (DG) methods are especially well suited for solving Eq. (26) and, more broadly, problems with Dirac delta distributions. The DG method solves the weak form of the problem, a natural setting for the delta distribution, and the solution’s non-smoothness can be “hidden” at an interface between subdomains. Our numerical scheme is based on the one described in Refs. [22, 39] for solving one-dimensional wave-like equations written in fully first-order form with source terms proportional to a Dirac delta distribution and its derivative(s). As such, we only summarize the key steps in the discretization and refer interested readers to those references for the details. After carrying out a spatial discretization using the nodal DG method, we integrate over time using the fourth order Runge Kutta (RK4) scheme.

A. The source-free method for $G = 0$

We partition the spatial domain into K non-overlapping subdomains defined by the partition points $\rho_0 < \rho_1 < \dots < \rho_K = s$ and denote $D^j = [\rho_{j-1}, \rho_j]$ as the j^{th} subdomain. In this one-dimensional setup, the points $\{\rho_i\}_{i=1}^{K-1}$ locate the internal subdomain interfaces, and we require

one of them to be the location of the Dirac distribution. Since we are solving a one-dimensional problem, the subdomains are line segments and neighboring subdomains will intersect at a point.

In each subdomain, all components of the solution vector U and matrices A , B , and V are expanded in a polynomial basis, which are taken to be degree- N Lagrange interpolating polynomials $\{\ell_i(\rho)\}_{i=0}^N$ defined from Legendre-Gauss-Lobatto (LGL) nodes. The time-dependent coefficients of this expansion (e.g., on subdomain j : $\pi_{20}^j(\tau, \rho) = \sum_{i=0}^N \pi_{20}^i(\tau) \ell_i(\rho)$) are the unknowns we solve for. Products of terms arising in Eq. (26) are represented through pointwise products of the interpolating polynomials at the LGL nodal points.

On each subdomain, we follow the standard DG recipe by requiring the residual

$$R_j(\tau, \rho) = \partial_\tau U^j + A^j \partial_\rho U^j + B^j U^j + V^j, \quad (39)$$

to satisfy

$$\int_{D^j} R_j \ell_i^j d\rho = \left[(F^j - F^*) \ell_i^j \right]_{x_{j-1}}^{x_j}, \quad (40)$$

for all basis functions – that is for all $i = 0, 1, \dots, N$. Here we use a superscript “ j ” for vectors and matrices whose components have been approximated by Lagrange interpolating polynomials. Eq. (40) features the physical flux vector, $F(U) = AU$ and the numerical flux F^* . The numerical flux is some yet-to-be-specified function $F^*(U^L, U^R)$, where U^L and U^R are, respectively, the left and right boundary values of the numerical solution defined on the interface between neighboring subdomains. To build a stable and convergent DG scheme the numerical flux must satisfy a few basic properties [46] such as consistency $F^*(U, U) = F(U)$. While there are many reasonable choices for the numerical flux, because of its simplicity and low cost-of-evaluation for our large, coupled system, we use the local Lax-Friedrichs (LLF) numerical flux. At each interface, the LLF flux is computed as

$$F^*(U^L, U^R) = \frac{1}{2} [F(U^L) + F(U^R)] - \frac{\lambda^{\text{LLF}}}{2} (U^R - U^L), \quad (41)$$

where λ^{LLF} is the maximum eigenvalue of the flux Jacobian matrix A evaluated at an interface; in our case $\lambda^{\text{LLF}} = 1$. The local Lax-Friedrichs flux is seen to be an average of the physical flux at the interface plus a dissipative part proportional to λ^{LLF} , which is necessary to stabilize the scheme.

We note that the integrals appearing in Eq. (40) can be pre-computed on a reference interval in terms of mass and differentiation matrices, leading to a coupled system of ordinary differential equations (see Eq. (47) of Ref. [39]) that can be integrated in time using RK4. A Courant-Friedrichs-Lewy condition restricts the largest stable timestep associated with explicit numerical integration of Eq. (40). For a DG scheme, it is known that $\Delta t_{\text{max}} \propto C \Delta x_{\text{min}} / \lambda_{\text{max}}$, where $\lambda_{\text{max}} = 1$ is the largest

wavespeed and Δx_{min} is the smallest distance between neighboring Legendre-Gauss-Lobatto points on the physical grid. The unknown scaling factor C is typically of order unity. Finally, the global solution is taken to be a direct sum of the local solutions defined on each subdomain, $U_h(\tau, \rho) = \bigoplus_{j=1}^K U_j(\tau, \rho)$.

B. Inverting \hat{E} and expressions at infinity

While not part of our DG scheme per se, an important numerical consideration is how to best invert \hat{E} . While one could numerically invert \hat{E} , we found that higher accuracies can be achieved through symbolic computations. This is, we compute $A = \hat{E}^{-1} \hat{A}$ symbolically, then export these expressions into code.

This symbolic approach works well for $\rho < s$. At $\rho = s$ the coordinate transformation (18) is singular yet, as remarked in Sec. IID, the coefficients of the first-order differential equation (20) are well behaved. However, special care is needed at $\rho = s$. To better appreciate the issue at hand, consider setting $M = a = 0$, then we end up with system (44). The terms on the right-hand-side – these are $(1 - H)$ and V – behave like r^{-2} as $r \rightarrow \infty$. Meanwhile, the matrix \hat{E}^{-1} behaves like r^2 as $r \rightarrow \infty$. Consequently, the coefficients and $\hat{E}^{-1}V$ need to be analytically supplied at $\rho = s$. This strategy continues to be applicable for the general case (with non-zero values of M and a) too. At grid points immediately to the left of $\rho = s$, the relevant coefficients in the partial differential operator might suffer from mild ill-conditioning; we experimented with variable precision computations but found no benefit.

C. Including the Dirac delta distribution

With a non-zero source term proportional to a Dirac delta distribution, the numerical flux evaluated at the interface $\rho = r_{*,p}$ will be modified through additional terms. The form of these new terms were derived in Eq. (58) of Ref. [39] and later extended in Ref. [22]. Consider a Dirac delta distribution located at the interface between elements D^{k_p} and $D^{k_{p+1}}$. The basic idea is to note that the DG method is a weak formulation of the differential equation, where the numerical solution is made to satisfy Eq. (40). When we collocate the $\delta(r_* - r_{*,p})$ with a subdomain interface, we are faced with evaluating two relevant integrals for the subdomain to the left and right of $r_{*,p}$. We enforce the usual selection property of the Dirac distribution when integrated over the union $D^{k_p} \cup D^{k_{p+1}}$, yet we are free to choose how the individual integrals contribute to the total one. Following Ref. [39], we carry out a preferred splitting according to the wave dynamics of the problem. Applying the procedure of Ref. [39] to

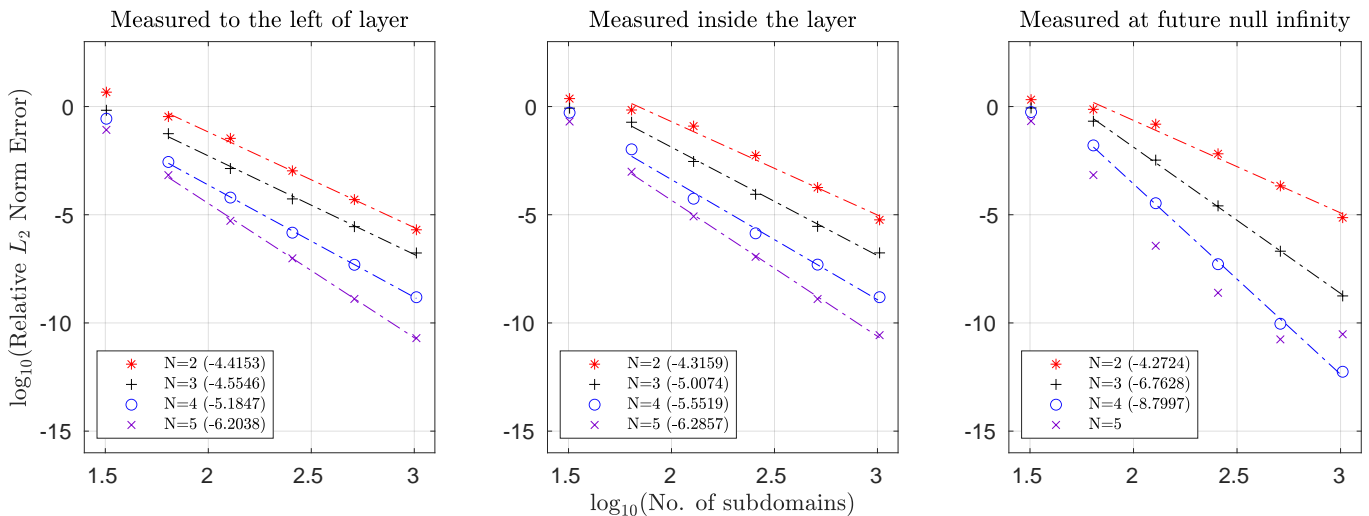


FIG. 1. Convergence of the numerical solution to the exact solution for the $\ell = 2$ wave equation using the hyperboloidal layer method. Errors are computed using a relative L_2 -norm computation Eq. (47). We consider convergence by increasing the number of subdomains K for approximating polynomial of degree $N = 2$ (red asterisk), $N = 3$ (black plus), $N = 4$ (blue circle), and $N = 5$ (purple cross). The error is measured at three locations on the spatial grid: before the start of the hyperboloidal layer (left panel), inside the hyperboloidal layer (middle panel), and at future null infinity given by $\rho = 50$ (right panel). For a fixed value of N , the approximation error decreases with a power law $E \propto K^{-p}$. We empirically measure p using a linear fit; our measured rates are shown in the legend. We find the convergence rate is similar to the “standard” one of $N + 1$ before and inside the layers. At future null infinity our scheme achieves superconvergence with a rate of nearly $2N + 1$. We note that convergence rates depend on the hyperboloidal layer’s compression function Eq. (19) (see Fig. 2), and the result here have been compiled with $P = 4$.

our problem we arrive at

$$-(F^*)_{\text{left, modified}}^{k_{p+1}} = -(F^*)_{\text{left}}^{k_{p+1}} + TP^+T^{-1}G(t), \quad (42a)$$

$$-(F^*)_{\text{right, modified}}^{k_p} = -(F^*)_{\text{right}}^{k_p} - TP^-T^{-1}G(t). \quad (42b)$$

The negative signs in front of each F^* instance can be understood by noting that the flux and source vectors are defined on different sides of the differential equation. Compare, for example, Eq. (40) and Eq. (26).

IV. NUMERICAL EXPERIMENTS

The numerical experiments documented in Sec .IV B and IV C set $M = 1$.

A. Verification of hyperboloidal layers: convergence and superconvergence

Our first experiment demonstrates exponential convergence of our solver throughout the hyperboloidal layer. Upon setting $a = M = q = 0$ ², the potential (10) be-

comes $V_{\ell m} = -\ell(\ell + 1)/r^2$ and $r_* = r$. And so Eq. (9) is just the ordinary flatspace wave equation:

$$\left[-\frac{\partial^2}{\partial t^2} + \frac{\partial^2}{\partial r^2} - \frac{\ell(\ell + 1)}{r^2} \right] \psi_{\ell m} = 0. \quad (43)$$

The first-order system in hyperboloidal coordinates is given from Eq. (20):

$$\dot{\psi}_{\ell m} = -\pi_{\ell m} \quad (44a)$$

$$\dot{\pi}_{\ell m} - H\dot{\phi}_{\ell m} = -(1 - H)\phi'_{\ell m} - \frac{\ell(\ell + 1)}{r^2}\psi_{\ell m} \quad (44b)$$

$$\dot{\phi}_{\ell m} - H\dot{\pi}_{\ell m} = -(1 - H)\pi'_{\ell m}. \quad (44c)$$

Due to the simple setting an exact, closed-form solution can be found [60]. Setting $\ell = 2$, the outgoing solution to Eq. (43) is

$$\psi(t, r) = f''(t - r) + \frac{3}{r}f'(t - r) + \frac{3}{r^2}f(t - r), \quad (45)$$

where $f(u)$ is an underlying function of $u = t - r$, the prime indicating differentiation in argument, and we have suppressed the harmonic indices. Specification of the profile function,

$$f(u) = \sin[f_0(u - u_0)]e^{-c(u - u_0)^2}, \quad (46)$$

² Clearly this setup does not correspond to an EMRI model. However, the resulting system (44) is an important special case for

which exact solutions can be computed. This allows for unambiguous code tests that are impossible otherwise.

determines a purely outgoing multipole solution [60]³. Here c characterizes the solution’s spatial extent, f_0 its “central” frequency, and u_0 its offset. A consequence of the hyperboloidal layer coordinate transformation, Eq. (21), is that $t - r = \tau - \rho$, which allows us to easily re-express the exact solution in (τ, ρ) coordinates.

We solve Eq. (44) (with $\ell = 2$) on $\rho \in [1, 50]$, with the layer at $R = 30$, set the final time $T = 50$, and choose a timestep $\Delta t = 10^{-5}$ sufficiently small enough such that the Runge-Kutta’s temporal error is well below the spatial discretization error. Upon setting $f_0 = 2$, $c = 1$, and $u_0 = -10$, we take the initial data from the exact solution evaluated at $\tau = 0$, which is (numerically) zero at the left boundary and the start of the layer $\rho = R$. At the left physical boundary point we choose numerical fluxes that weakly enforce simple Sommerfeld (outgoing) boundary conditions, which are sufficient for our purposes as the solution never impinges upon this boundary. Because of the property of the hyperboloidal layers, no boundary conditions are needed at $\rho = 50$.

We now check the convergence of our numerical solution against the exact solution when using hyperboloidal layers. It is well known that for a fixed value of polynomial degree N , the approximation error (when computed in the L_2 norm over the spatial grid at a fixed time T) typically decreases as a power law with an anticipated rate of $N + 1$ for smooth solutions. We say this is “anticipated” because it follows from standard results of polynomial approximation theory and has nothing to do with the DG scheme, which can modify the expected rate depending on the system and various method choices. Without using hyperboloidal layers our numerical scheme (for the ordinary wave equation) is identical to the one of Ref. [22] where the expected convergence rate of $N + 1$ is demonstrated in Fig. 3 of that reference; similar results hold for non-linear problems [61].

We now show that our numerical approximation error continues to decay with a rate of $N + 1$ when using the method of hyperboloidal layers. Furthermore, at certain locations of the grid we achieve *superconvergent* rates of $2N + 1$. We report the numerical error as a relative L_2 norm

$$E_{N,K}(\rho) = \frac{\int_0^T |\psi_{\text{num}}(\tau, \rho) - \psi_{\text{exact}}(\tau, \rho)|^2 d\tau}{\int_0^T |\psi_{\text{exact}}(\tau, \rho)|^2 d\tau} \quad (47)$$

taken over time at a fixed value of ρ . The numerical solution ψ_{num} is computed using a degree N approximating polynomial on a grid of K subdomains.

Fig. 1 shows the scheme’s rate of convergence as N and K are varied. We measure the error before the layer at $\rho = 15$ (left panel), inside the layer at $\rho = 40$ (middle panel), and at future null infinity at $\rho = 50$ (right panel). For the first two cases these values of ρ correspond to

grid points that do not lie on the rightmost side of a subdomain. The scheme’s rate of convergence is consistent with our $N + 1$ expectation. By comparison, the rate of at future null infinity is found to be $2N + 1$. This is a hallmark of a superconvergent DG scheme [62–64], at which certain grid points (in this case, the outflow boundary is also a Radau nodal point) converge at a higher rate than that of other grid points. Finally, Fig. 2 shows the scheme’s (super)convergence depends on the coordinate transformation (19) that defines the hyperboloidal layer. Noting that the transformation is parameterized by a positive integer P , Fig. 2 shows a loss of convergence when the hyperboloidal layer’s differentiability is too low ($P = 2$) or P is odd.

Because the far-field waveform reaching gravitational-wave detectors is taken to be at future null infinity, superconvergence allows our scheme to obtain highly accurate waveforms for comparatively sparse computational grids. Furthermore, because the largest stable timestep scales as N^{-2} , our high-order waveform computation can be achieved with a larger step. For example, setting $N = 4$ we achieve 9th order convergence. Without superconvergence this would only be possible with $N = 8$, which translates into $4\times$ larger timesteps. We note that superconvergence is not a property of hyperboloidal layers, but rather our DG scheme. Yet the two work well together as $\rho = s$ is both a super-convergent point and exactly where we need to record the far-field waveform after applying the method of hyperboloidal layers.

Finally, Fig. 3 demonstrates the spectral convergence of our method as applied to Eq. (44) (our preferred first-order reduced system; denoted “System 1” in the legend) and Eq. (D3) (denoted “System 2” in the legend). We observe the problematic “System 2” loses convergence much sooner than “System 1”, in particular well before round-off error is expected to show up. While a complete understanding of this issue is still lacking, some observations are reported in App. D. For these experiments, we use a fixed number of $K = 128$ subdomains and plot the error (47) as a function of N and for each N . We have chosen a $\Delta t = 0.00001$ to ensure temporal error is well below the spatial discretization error.

B. Verification of Price tails

The late time decay behavior of scalar field perturbations around a Kerr black hole were first shown in Ref. [65]. At late times, after the the exponential decay of ringdown, the field decays as a power law t^n . In this subsection, we perform a series of experiments to test our code by comparing to results from the literature. In the legends of Figs. 4 and 5, the first value in the parentheses represents the expected behavior. We use two methods to extract a value of n from our numerical data: (i) power law fit evaluated at 100,000 (the second number in the parentheses of each legend) and (ii) each figure also includes an inset where the decay rate is computed from a finite-

³ Eq. (53) from Ref.[60] (which is Eq. (60) in arXiv version 1) has a typo. This equation is corrected in arXiv version 2.

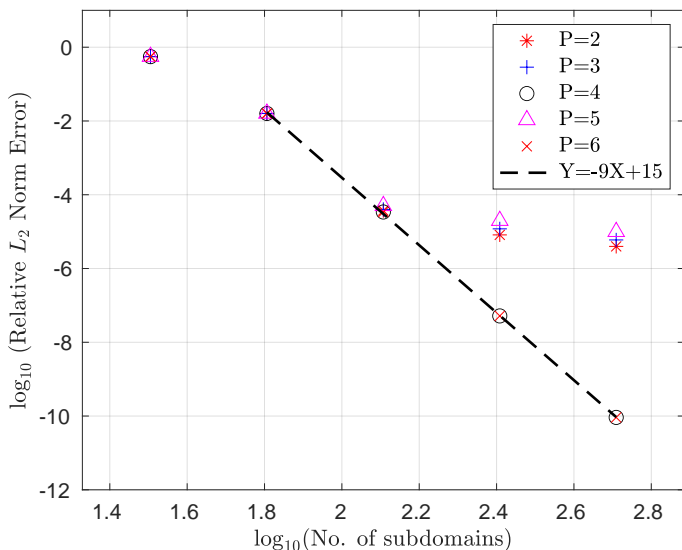


FIG. 2. Convergence of the numerical solution to the exact solution for the $\ell = 2$ wave equation using the hyperboloidal layer method. Errors are computed using a relative L_2 -norm computation Eq. (47). We consider convergence by increasing the number of subdomains K for an approximating polynomial of degree $N = 4$. The error is measured at future null infinity given by $\rho = 50$; as shown in Fig. 1 (right panel) our DG scheme exhibits superconvergence (i.e. the errors decay faster than $E \propto K^{-(N+1)}$) at this grid location. We now consider how the value of P that defines the hyperboloidal layer’s compression function Eq. (19) can impact (super)convergence. We consider $P = 2$ (red asterisk), $P = 3$ (blue plus), $P = 4$ (black circle), $P = 5$ (purple triangle), and $P = 6$ (red cross). We see that convergence is lost whenever the coordinate transformation’s degree of differentiability is too low (e.g. $P = 2$) or P is odd. For visual assistance, the dashed-black line shows the expected superconvergence decay rate for $N = 4$ as shown in the rightmost panel of Fig. 1. We find that our method maintains superconvergence for both $P = \{4, 6\}$. $\Delta t = 10^{-5}$.

difference approximation to the logarithmic derivative $n = \partial_{\ln \tau} \ln(\psi_{\ell m}(\tau))$.

We provide initial data to the scalar field at some point away from the black hole event horizon but well before the hyperboloidal layer starts. The solution is then extracted as a time series at a location inside the layer and at \mathcal{I}^+ . This also acts as an important test for the hyperboloidal layer method.

Finally, we note that some results of this section have been compiled using the alternative first-order reduced system discussed in App. D; this shows that although the alternative system is problematic for certain studies (cf. Sec. IV C and Sec. IV A) it can be used when high-accuracy is not required.

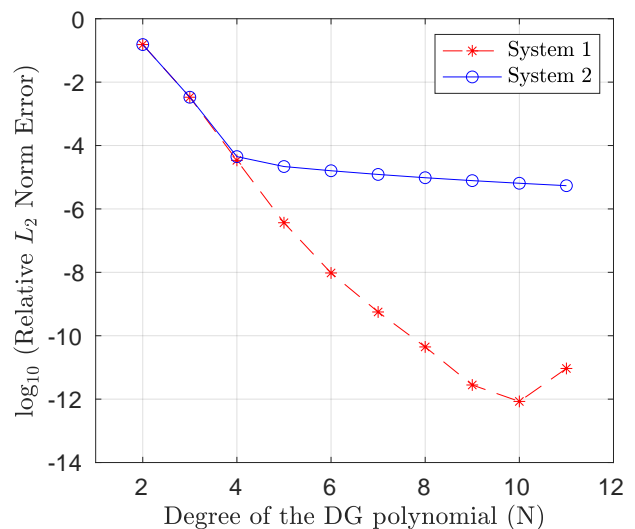


FIG. 3. Spectral (exponential) convergence of the $\ell = 2$ hyperboloidal layers experiment described in Sec. IV A. Errors have been computed from $\psi_{\text{num}}(\tau, \rho = 50)$, which is the signal that reaches future null infinity \mathcal{I}^+ . Convergence results are reported for system 1 (dashed-red line; our preferred first-order reduced system (44) that is symmetric hyperbolic) and system 2 (solid-blue line; an alternative first-order system (D3) that is discussed in App. D). For system 1, we see excellent convergence with N until round-off error effects become noticeable around 10^{-12} . We find that our DG scheme solving system 2 is unable to obtain the expected accuracy that should be achievable by double-precision. A complete understanding of this issue is still lacking; see App. D.

1. Price tails on Schwarzschild

For our first test we perturb the scalar field around the background Schwarzschild spacetime with non-zero momentum initial data,

$$\psi_{\ell m} = 0, \quad \pi_{\ell m} = \frac{1}{\sqrt{2\pi}10^2} \exp\left(\frac{-(\rho - 30)^2}{2\pi 10^2}\right), \quad (48)$$

and where $\phi_{\ell m} = \partial_{r_*} \psi_{\ell m}$. We solve Eq. (20) (with $\ell = 2$ and $M = 1$) on $\rho \in [-200, 1200]$ with the layer at $R = 150$. We use $K = 400$ subdomains and on each subdomain the solution is approximated by a degree $N = 10$ polynomial. The time step is set to $\Delta t = 0.0866$. In Fig. 4, we show the solution recorded as a time series at $r_* = 500$ (left panel) and at \mathcal{I}^+ (right panel). At late times we empirically measure the decay rate of solution and quote this value in the parentheses of the figure’s label. In the inset figure, we also report the local power index and show the expected rate (as a horizontal line) based on Price’s Law [65]. Our measured tail decay rates are consistent with the theoretically known values at both a finite distance and \mathcal{I}^+ [66].

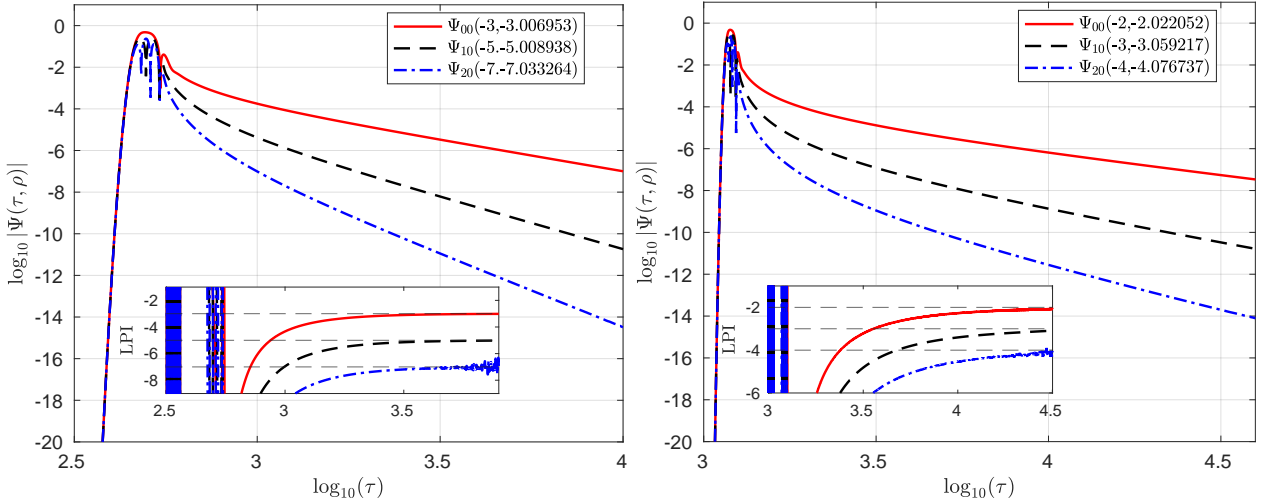


FIG. 4. Late time tail behavior of a scalar field evolving on a Schwarzschild spacetime with non-zero momentum initial data, Eq. (48). The $\ell = 0$ (solid red), $\ell = 1$ (dashed black), and $\ell = 2$ (dashed-dot blue) modes are shown. The inset figure shows the local power index (LPI) approaching the theoretically expected values shown as a dashed horizontal line. The parantheses values in the legend represent the expected tail rate and the numerical fit values. **Left panel:** Late-time Schwarzschild tails for signals extracted at $r_* = 500$ (inside the hyperboloidal layer) showing the expected $-2\ell - 3$ power law behavior. **Right panel:** The signal extracted at the right boundary which, from hyperboloidal layers compactification is the null infinity \mathcal{I}^+ . We find the power-law behavior follows the expected $-\ell - 2$ rate.

2. Price tails on Kerr

Unlike the Schwarzschild case, a full understanding of Price tails in Kerr spacetime was not developed until relatively recently [67–72] (the reader is referred to the detail therein). Consider the situation where ℓ' is the mode where we set the initial data (assuming non-zero momentum), and ℓ is the mode excited through coupling. As proposed in Ref. [71] and later shown in Ref. [72], except for the case in which ℓ' is the slowest decaying mode (for which case the decay rates are given by $-n = \ell' + \ell + 3$), all other azimuthal modes decay along $r = \text{const}$ (approaching future timelike infinity i^+) according to $-n = \ell' + \ell + 1$. Ref. [71] also found the decay rate along future null infinity \mathcal{I}^+ , specifically, $-n^{\mathcal{I}^+} = \ell + 2$ if $\ell \geq \ell'$, and $-n^{\mathcal{I}^+} = \ell$ if $\ell \leq \ell' - 2$.

In Fig. 5 we repeat our Schwarzschild tails experiment but now setting $a = 0.99995$. We solve on the domain $\rho \in [-2100, 400]$ with the start of the hyperboloidal layer at $R = 149.3500$. We use $K = 400$ subdomains and on each subdomain the solution is approximated by a degree $N = 15$ polynomial. The time step is set to $\Delta t = 0.0761$. To facilitate a direct comparison with previous work, we choose our initial data to match that of Ref. [70]. In particular, we provide a non-zero $(2, 0)$ mode perturbation that, through mode coupling, excites the $(0, 0)$ and $(4, 0)$ modes. Technically all $m = 0$, even ℓ modes will be excited, but we only consider nearest neighbor coupling for this experiment; see Sec. II E. Our measured rates are consistent with known results.

As a final test, we extend this experimental setup (now using $N = 10$, $K = 400$, and $\Delta t = 0.0436$) for a range of

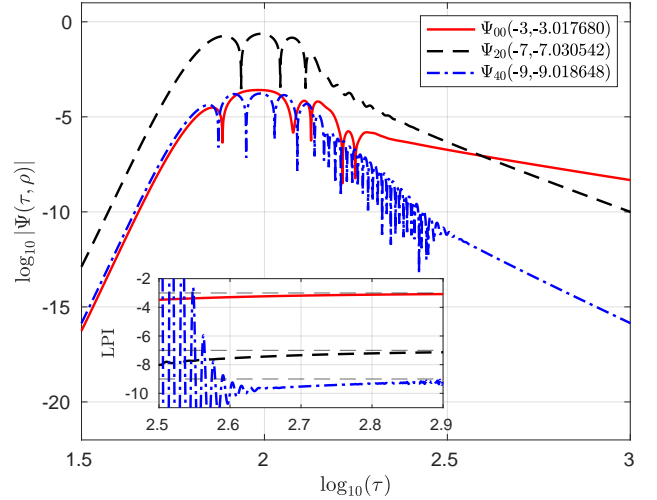


FIG. 5. Late time tail behavior of a scalar field evolving on a Kerr spacetime with a spin of $a = 0.99995$. The initial data is set as $\psi_{20} = 0$, $\phi_{20} = 0$, and $\pi_{20} = \frac{1}{\sqrt{2\pi 6^2}} \exp\left(\frac{-(\rho-25)^2}{2\pi 6^2}\right)$, while the $(4, 0)$ and $(0, 0)$ modes are 0. The solution is then extracted at $r_* = 100$. The numbers in the parentheses show the expected rate vs the calculated decay rate of the perturbations.

non-zero (ℓ', m) mode data and report the measured decay rate of the coupled (ℓ, m) modes. Table I summarizes numerical experiments while using a spin value of $a = 0.8$.

Initial ℓ', m mode	Projected $\ell = 0$	Projected $\ell = 1$	Projected $\ell = 2$	Projected $\ell = 3$	Projected $\ell = 4$	Projected $\ell = 5$
(0,0)	-3.012	*	-5.027	*	-7.449	*
(1,1)	*	-5.008	*	-7.016	*	-9.710
(2,0)	-3.010	*	-7.013	*	-9.004	*
(2,2)	*	*	-7.016	*	-9.049	*
(3,1)	*	-5.009	*	-9.013	*	-11.024
(4,0)	-5.022	*	-7.010	*	-11.255	*
(4,2)	*	*	-7.012	*	-11.009	*

TABLE I. We reproduce the $(\ell', m) \rightarrow (\ell, m)$ scattering matrix from Ref. [70] where they verified the late time tail behavior of scalar fields in the Kerr background using quad precision. We set the spin on the primary black hole as $a = 0.8$. The expected behavior is $\ell' + \ell + 1$ if $\ell < \ell'$ and $\ell' + \ell + 3$ if $\ell \geq \ell'$. We get the expected behavior with less than 1% of error. Since the higher modes are very weakly coupled to the initial ℓ' mode, double-precision round-off errors prevent us from obtaining accurate computations of the power-law behavior for certain couplings. More accurate results can be obtained with quad-precision floating-point computations, which we hope to consider in the future.

C. Fluxes from a scalar-charged particle in circular orbit

1. Fluxes on Schwarzschild

This subsection compares our circular orbit energy fluxes (38) to those obtained by other authors and codes. For our simulations, we have typically chosen $M = 1$, and we solve Eq. (20) with a distributional source term given by Eq. (14). Our physical domain $\rho \in [-100, 200]$ is partitioned into 200 subdomains and on each subdomain we approximate the solution with a degree $N = 10$ polynomial. We set the final time $T = 8000$, and the time step $\Delta t = 0.0018$. As is common practice, we supply trivial (zero) initial data. We note that supplying trivial initial data is commonly done because (i) the exact initial data is unknown and (ii) the expectation is that over long enough times the impact of incorrect initial data will propagate away as so-called junk radiation [73]. Trivial initial data is inconsistent with the distributional forcing terms (14), so we smoothly turn on the source term with a ramp-up function. We take our ramp-up function to be Eq. C1 of Ref. [39] with parameter values $\tau = 400$ and $\delta = 0.00025$. To achieve high accuracies for some of the higher harmonic modes, we sometimes deviate from these default settings.

Before presenting our numerical results, we remark on potential sources of error. With the numerical setup described above, the relative error associated with our numerical solution before the start of the hyperboloidal layer is better than 10^{-10} , which is sufficient for our purposes. At \mathcal{S}^+ , where the energy flux is computed, we encounter two additional sources of error: spurious junk due to trivial initial data and setting the hyperboloidal layer's width. These two sources of (systematic) error are quantified in Fig. 6. In this experiment, we consider a high-resolution numerical computation of the (2,2)-mode energy flux $\dot{E}_{\text{DG}}^{22}(\tau)$ from a particle in circular orbit located at $r_{*,p} = 12.7725887222397$ and our domain is $\rho \in [r_{*,p} - 200, r_{*,p} + 200]$. For a fixed location of the hyperboloidal layer's start ($\rho = R$), the figure shows

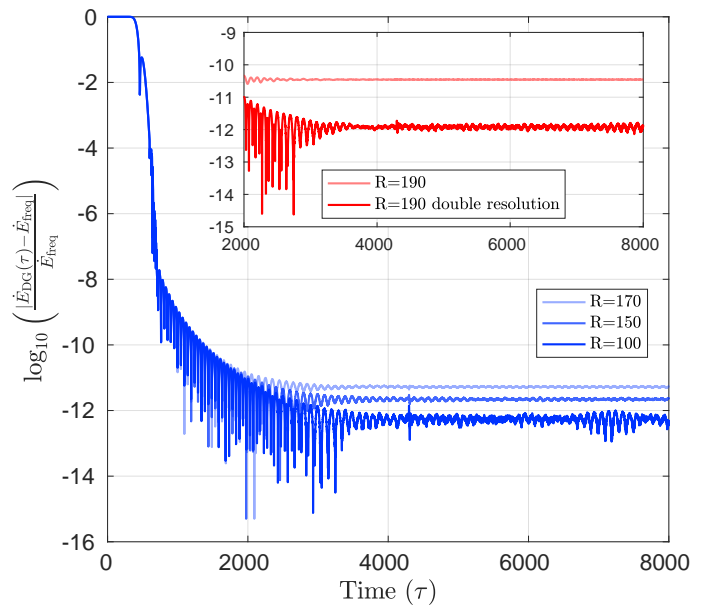


FIG. 6. Relative error in the (2,2)-mode energy flux computed with our time-domain solver (\dot{E}_{DG}^{22}) compared with a frequency-domain solver (\dot{E}_{FR}^{22}). We find that increasing the hyperboloidal layer's width helps in achieving higher accuracy scalar fluxes in the (2,2) mode. Here R is the start of the layer, so larger values of R correspond to narrower layers. We also find that spurious junk tails, due to inconsistent initial data, need sufficient time to decay away before high-accuracy measurements can be made. For this experiment $N = 9$, $K = 100$ and $\Delta t = 0.010461$ were kept fixed for all values of R , and we set $K = 200$ when using “double resolution”.

the agreement between our DG scheme and a frequency-domain solver [74, 75] becomes better as we wait longer. Indeed, for each R we plot the relative error computed as

$$|\dot{E}_{\text{DG}}^{\ell m}(\tau) - \dot{E}_{\text{FR}}^{\ell m}| / |\dot{E}_{\text{FR}}^{\ell m}|, \quad (49)$$

where $\dot{E}_{\text{FR}}^{\ell m}$ is the energy flux computed with a frequency-domain solver and $\dot{E}_{\text{DG}}^{\ell m}(\tau)$ is the time-domain DG solver's value. We see that at early times the solution is highly con-

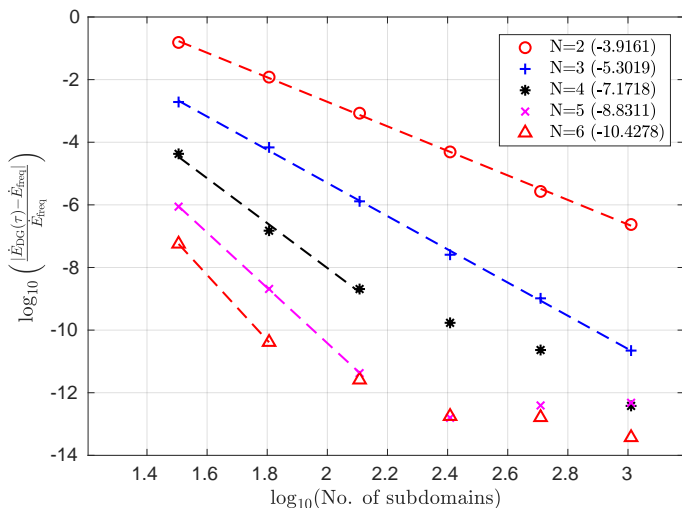


FIG. 7. Superconvergence of numerically computed energy fluxes from a particle in circular orbit at $r_p = 10M$ on Schwarzschild. Relative errors in the (2,2)-mode energy flux are computed with our time-domain solver ($\dot{E}_{N,K}^{22}$) and compared with a frequency-domain solver ($\dot{E}_{\text{freq}}^{22} = 3.369977470603454 \times 10^{-6}$). We consider convergence by increasing the number of subdomains K for approximating polynomial of degree $N = 2$ (red circles), $N = 3$ (blue plus), $N = 4$ (black asterisk), $N = 5$ (purple cross), and $N = 6$ (red triangle). We find the convergence rate is between $2N - 1$ to $2N$, which is faster than the “standard” one of $N + 1$. Similar superconvergence was obtained for the ordinary wave equation using hyperboloidal layers; see Fig. 1.

taminated by spurious junk. Achieving a high-accuracy solution requires that we wait sufficiently long for the spurious “junk tails” to decay away. As noted in Ref. [73], because tails at \mathcal{I}^+ decay more slowly, one must wait even longer (as compared to finite-radius measurements) for these transients to die off.

Fig. 6 also shows that as $R \rightarrow s$ (ie the layer’s width goes to zero) our solution quality degrades. We believe this is due to sharper gradients that stem from the compression function Ω , which makes it harder for the numerical scheme to approximate the solution for a fixed grid resolution. For example, setting $R = 100$ (where the layer’s width is ≈ 110) we find the energy flux computation is accurate to a relative error on the order of 10^{-12} . Keeping the grid resolution fixed, we see that the error in the flux computation increases as the layer’s width shrinks. When $R = 190$ (where the layer’s width is ≈ 22) the error is now $\approx 5 \times 10^{-11}$, yet doubling the number of subdomains improves the solution quality allowing for energy flux computations to again obtain relative errors on the order of 10^{-12} . To achieve efficient numerical schemes it would be helpful to have criteria for setting the layer’s width given properties of the problem, but this is currently unavailable in the literature.

Having properly accounted for these sources of error, Table II compares the energy flux (computed from high resolution runs) to values computed using as frequency-

(ℓ, m)	Alg.	Energy Flux ($\dot{E}^{\ell m}/q^2$)	Relative Error
System 1			
(2,2)	FR	$2.1676683889035 \times 10^{-6}$	1.7×10^{-12}
	DG	$2.1676683889071 \times 10^{-6}$	
(4,2)	FR	$3.7609900151243 \times 10^{-11}$	1.3×10^{-10}
	DG	$3.7609900156162 \times 10^{-11}$	
(5,3)	FR	$8.8539629089954 \times 10^{-13}$	2.7×10^{-10}
	DG	$8.8539629113568 \times 10^{-13}$	
(9,7)	FR	$3.5707073944101 \times 10^{-14}$	3.2×10^{-11}
	DG	$3.5707073942955 \times 10^{-14}$	
(15,15)	FR	$2.1814822732028 \times 10^{-16}$	7.8×10^{-11}
	DG	$2.1814822730317 \times 10^{-16}$	
System 2			
(2,2)	FR	$2.1676683889035 \times 10^{-6}$	3.5×10^{-7}
	DG	$2.1676691548376 \times 10^{-6}$	
(4,2)	FR	$3.7609900151243 \times 10^{-11}$	1.1×10^{-6}
	DG	$3.7609939802703 \times 10^{-11}$	

TABLE II. Mode-by-mode energy fluxes from a circular orbit around a Schwarzschild black hole. The table compares our time-domain solver results (Alg.=DG) with frequency-domain (FR) results (Alg.=FR) computed by a code made publicly available through the Black Hole Perturbation Tool Kit (BHPTK). For all modes except (5,3), the particle is located at $r_* = 10.99332834601232$, while for the (5,3) we use $r_* = 16.09469709319520$. Relative errors are computed as $|\dot{E}_{\text{DG}}^{\ell m} - \dot{E}_{\text{FR}}^{\ell m}|/|\dot{E}_{\text{FR}}^{\ell m}|$. Results are reported for system 1 (our preferred first-order reduced system (44) that is symmetric hyperbolic) and system 2 (an alternative first-order system (D3) that is discussed in App. D). We find that DG schemes solving system 2 are unable to obtain accuracies that should be achievable by double-precision. A complete understanding of this issue is still lacking.

domain solver [75] implemented within the Black Hole Perturbation Toolkit [74]. These frequency-domain results rely on the appropriate boundary value problems in the frequency domain and allows for a direct, non-trivial comparison between methods. Finally, Fig. 7 shows the rate of convergence in our DG scheme’s energy flux computation (at time $4000M$ after junk radiation has left the system) as N and K are varied while the timestep $\Delta t = 0.010460592$ is kept fixed. As the energy flux is computed at future null infinity we anticipate superconvergent rates similar to those observed for the flatspace wave equation; see the rightmost panel of Fig. 1. For DG methods the numerical error is expected to decrease exponentially fast, $E \propto K^{-p}$, where $p = N + 1$ is the standard convergence rate. Fig. 7 shows the rate of convergence to be much faster than $N + 1$, and about 1 order of convergence less than what’s shown in Fig. 1. This discrepancy can be understood by noting that the errors shown in Fig. 1 are for Ψ , while for the energy flux computation the errors are due to $\pi = -\partial_t \psi$.

V. SUMMARY AND FUTURE WORK

This paper presents a new numerical method for solving the distributionally-forced $s = 0$ Teukolsky equation (scalar waves on Kerr) that models extreme mass ratio inspirals (EMRIs) in a Kerr spacetime. Our method uses a nodal discontinuous Galerkin (DG) approach that expands the solution in spherical harmonics and recasts the sourced Teukolsky equation as a set of coupled, fully-first order one-dimensional symmetric hyperbolic equations. This approach allows us to correctly account for the Dirac delta distribution using a modified numerical flux and achieve global spectral accuracy even at the source's location. Furthermore, we use the hyperboloidal layer method to connect the near field to future null infinity, providing direct access to the far-field waveform. Our numerical experiments demonstrate the accuracy and efficiency of the method, including convergence tests against exact solutions, energy luminosities for circular orbits, and the scheme's superconvergence at future null infinity.

Our method has several advantages over existing time-domain solvers for the distributionally-forced Teukolsky equation. First, it does not introduce small-length scales near the smaller black hole, which can be a significant source of systematic error in other time-domain solvers. Combined with spectral accuracy at the source's location, our DG scheme and code should be well-suited for self-force calculations that require highly-accuracy numerics at the location of delta distribution. Its also worth noting that when computing gravitational self-force effects a suitable regularization procedure must be used. Regularization techniques have been well-developed for the spherical harmonic modes. Yet in frequency-domain Kerr calculations, spheroidal harmonics are exclusively used, which in turn requires projecting onto a spherical harmonic basis before the regularization step can be applied. In our method, we directly solve for the spherical harmonic modes, thereby avoiding this complicated intermediate step. Second, it achieves global spectral accuracy (in fact, superconvergence), which is critical for accurately capturing the complex dynamics of extreme mass ratio inspirals both at the smaller black hole's location and in the far field. Finally, our method provides direct access to the far-field waveform, a key output of the simulation that can be compared with data from upcoming space-based gravitational wave detectors.

As a byproduct of our work, we have compiled numerical evidence that when combined with the hyperboloidal layer method, one seemingly reasonable choice of the first-order reduction variable appears to be problematic. This issue shows up in different settings, such as calculating scalar fluxes at future null infinity or when comparing to exact solutions of the ordinary wave equation. In all settings, the numerical solution's accuracy saturates at about 5 to 6 digits irrespective of the timestep or grid resolution. On the other hand, with a better choice of auxiliary variable, we are able to achieve the expected decay of numerical error to better than 12 digits of accu-

racy. We also show that the resulting first-order system is symmetric hyperbolic in certain cases.

There are several avenues for future work that could extend and improve our methodology. One important direction is the extension of our method to handle the $s = \pm 2$ Teukolsky equation, which are needed for modeling gravitational waves from EMRI systems. Another area for future work is the development of methods to handle eccentric orbits using a time-dependent coordinate transformation, which has been worked out in simpler settings [39]. The methods presented in this paper assume circular orbits, but eccentric orbits are common in real astrophysical EMRI systems and can significantly impact the gravitational wave signal's morphology. Finally, there is also potential for further improving the accuracy and efficiency of our method by exploring higher-order time-stepping methods or adaptive mesh refinement.

ACKNOWLEDGMENTS

We thank Anil Zenginoglu for discussions on first-order reductions and hyperboloidal layers, and Jennifer Ryan for discussions on superconvergence. We thank Som Bishoyi, Zachariah Etienne, Alfa Heryudono, Scott A. Hughes, Harald Pfeiffer, Leo Stein, Saul Teukolsky, Alex Vano-Vinuales, Niels Warburton, and Barry Wardell for helpful discussions throughout the project. We also thank Karoly Csukas and Hannes Rüter for their valuable feedback on an earlier draft of this paper. The authors acknowledge support of NSF Grants PHY-2106755 and PHY-2307236 (G.K), DMS-1912716 and DMS-2309609 (S.F, S.G, and G.K), AFOSR Grant No. FA9550-18-1-0383 (S.G) and Office of Naval Research/Defense University Research Instrumentation Program (ONR/DURIP) Grant No. N00014181255. This material is based upon work supported by the National Science Foundation under Grant No. DMS-1439786 while a subset of the authors were in residence at the Institute for Computational and Experimental Research in Mathematics in Providence, RI, during the Advances in Computational Relativity program. Some of the simulations were performed on the UMass-URI UNITY supercomputer supported by the Massachusetts Green High Performance Computing Center (MGHPCC). We also thank ChatGPT for writing the first draft of the conclusion (and only the conclusion) of this paper.

Appendix A: Mode-coupling coefficients

When expanding the $s = 0$ Teukolsky equation (1) in spherical harmonics, we encounter a term $\sin^2 \theta Y_{\ell m}$ that is responsible for mode coupling. To re-expand this term with spherical harmonics

$$\sin^2 \theta Y_{\ell m} = c_{\ell m}^{\ell-2} Y_{\ell-2, m} + c_{\ell m}^{\ell} Y_{\ell m} + c_{\ell m}^{\ell+2} Y_{\ell+2, m} \quad (\text{A1})$$

$$= C_{++}^{\ell-2} Y_{\ell-2, m} + C_0^{\ell} Y_{\ell m} + C_{--}^{\ell+2} Y_{\ell+2, m} \quad (\text{A2})$$

we need expressions for the mode-coupling coefficients. These can be found from either Ref. [43] or Ref. [52], where the latter considered coupling between associated Legendre polynomials, $P_\ell^m(\cos\theta)$. We follow Ref. [43], and in line (A2) we switch from our paper's notation to the notation used by Ref. [43]. Quoting the relevant results from Ref. [43], we have

$$\begin{aligned} C_{++}^\ell &= -c_+^{\ell+1} c_+^\ell, \\ C_0^\ell &= 1 - (c_-^\ell)^2 - (c_+^\ell)^2, \\ C_{--}^\ell &= -c_-^{\ell-1} c_-^\ell, \end{aligned} \quad (\text{A3})$$

where

$$c_-^\ell = \left[\frac{(\ell^2 - m^2)}{(2\ell - 1)(2\ell + 1)} \right]^{1/2}, \quad c_+^\ell = c_-^{\ell+1}. \quad (\text{A4})$$

Appendix B: Matrix form of the full system (20)

We now consider the matrix form for the general system (20) for any combination of ℓ_{\max} , m and ℓ -mode type = {odd, even}. The even and odd ℓ modes decouple so

their governing systems can be analyzed separately. For concreteness, consider (for a fixed value of m) the even ℓ -mode sector, where $\ell = \ell_{\min}, \ell_{\min} + 2, \dots, \ell_{\max}$. First, we split our solution vector $U_{\ell_{\max}m}$ into subvectors

$$\begin{aligned} \vec{\pi}_{\ell_{\max}m} &= [\pi_{\ell_{\min}m}, \pi_{(\ell_{\min}+2)m}, \dots, \pi_{\ell_{\max}m}]^T, \\ \vec{\phi}_{\ell_{\max}m} &= [\phi_{\ell_{\min}m}, \phi_{(\ell_{\min}+2)m}, \dots, \phi_{\ell_{\max}m}]^T, \end{aligned}$$

which allows us to write $U_{\ell_{\max}m} = [\vec{\pi}_{\ell_{\max}m}, \vec{\phi}_{\ell_{\max}m}]$. We now use block notation to index vectors, for example $U_\pi^{\ell_{\max}m} = \vec{\pi}_{\ell_{\max}m}$. With this new notation, the matrices defining the first-order system, Eq. (25) can be partitioned as

$$E = \begin{pmatrix} E_{\pi\pi} & E_{\pi\phi} \\ E_{\phi\pi} & E_{\phi\phi} \end{pmatrix}, \quad \hat{A} = \begin{pmatrix} \hat{A}_{\pi\pi} & \hat{A}_{\pi\phi} \\ \hat{A}_{\phi\pi} & \hat{A}_{\phi\phi} \end{pmatrix}. \quad (\text{B1})$$

The block-wise components of \hat{A} are $\hat{A}_{\pi\pi} = \hat{A}_{\phi\phi} = 0$ and $\hat{A}_{\pi\phi} = \hat{A}_{\phi\pi} = (1 - H)\mathbf{I}$, where \mathbf{I} is the identity matrix. The block-wise components of E are $E_{\pi\phi} = E_{\phi\pi} = -H\mathbf{I}$, $E_{\phi\phi} = \mathbf{I}$, and the tridiagonal matrix

$$E_{\pi\pi} = \begin{pmatrix} 1 - fc_{\ell_{\min},m}^{\ell_{\min}} & -fc_{\ell_{\min}+2,m}^{\ell_{\min}} & 0 & 0 & 0 & 0 \\ -fc_{\ell_{\min},m}^{\ell_{\min}+2} & 1 - fc_{\ell_{\min}+2,m}^{\ell_{\min}+2} & -fc_{\ell_{\min}+4,m}^{\ell_{\min}+2} & 0 & \vdots & \vdots \\ 0 & -fc_{\ell_{\min}+2,m}^{\ell_{\min}+4} & 1 - fc_{\ell_{\min}+4,m}^{\ell_{\min}+4} & -fc_{\ell_{\min}+6,m}^{\ell_{\min}+4} & 0 & 0 \\ 0 & 0 & \ddots & \ddots & \ddots & 0 \\ \vdots & \vdots & \vdots & \vdots & \ddots & \vdots \\ 0 & 0 & 0 & -fc_{\ell_{\max}-4,m}^{\ell_{\max}-2} & 1 - fc_{\ell_{\max}-2,m}^{\ell_{\max}-2} & -fc_{\ell_{\max},m}^{\ell_{\max}-2} \\ & & & 0 & -fc_{\ell_{\max}-2,m}^{\ell_{\max}} & 1 - fc_{\ell_{\max},m}^{\ell_{\max}} \end{pmatrix}. \quad (\text{B2})$$

The matrix structure for the odd ℓ -modes is identical. From properties documented in App. A, we have $c_{\ell,m}^{\ell+2} = c_{(\ell+2),m}^\ell$ which implies $E_{\pi\pi}$ is symmetric. Therefore, E is also symmetric. That \hat{A} is symmetric follows from straightforward inspection.

Finally, we consider the flux Jacobian matrix A defined from Eq. (26). In terms of block-wise components we have

$$\frac{A}{1 - H} = \left(\begin{array}{c|c} H(E_{\pi\pi} - H^2)^{-1} & (E_{\pi\pi} - H^2)^{-1} \\ \hline (\mathbf{I} - H^2 E_{\pi\pi}^{-1})^{-1} & H(\mathbf{I} - H^2 E_{\pi\pi}^{-1})^{-1} E_{\pi\pi}^{-1} \end{array} \right), \quad (\text{B3})$$

where $E_{\pi\pi}^{-1} E_{\pi\pi} = \mathbf{I}$. We see that in general A is not a symmetric matrix, even though $E_{\pi\pi}^{-1}$ is. By considering $H = 0$ we see that each of the four blocks of A are symmetric when working in the original t and r_* coordinates.

Appendix C: Eq. (20) as a symmetric hyperbolic system

With an explicit expression for the matrices of our problem given in App. B, we now show conditions under which the first-order system (20) is symmetric hyperbolic. Recall that to study a first-order system's hyperbolicity classification it is sufficient to consider the principle part of the differential equations,

$$\hat{E}\dot{U} + \hat{A}U' + \dots = 0, \quad (\text{C1})$$

$$\dot{U} + AU' + \dots = 0, \quad (\text{C2})$$

where the variable-coefficient matrices $A(\rho)$, $\hat{E}(\rho)$, and $\hat{A}(\rho)$ depend on the spatial independent variable ρ and "... denotes lower-order terms (ie. it does not include any term proportional to \dot{U} or U'). System (C1) represents the form of our original system (20)'s principle part after we put it into matrix form (25) where the matrices are shown explicitly in App. B. System (C2) is the result of

inverting \hat{E} , leading to the system (26) that we discretize with the DG method.

One important question is whether or not this system constitutes a well-posed initial-boundary-value problem (IBVP). That is, given sufficiently smooth initial conditions $U(0, \rho)$ and dissipative boundary conditions, the L_2 norm of U can be bounded by norms taken over the initial data and boundary conditions [76–78]. Well-posedness for linear, variable-coefficient systems like ours can be shown if the problem is symmetric hyperbolic system [78]. This condition is sometimes stated as follows: the system (C2) is symmetric hyperbolic if $A(\rho)$ is a symmetric matrix at all values of ρ in the physical domain [78]. Direct inspection of Eq. (B3) shows that this is not the case. However, a similar well-posedness result follows if we show our system (C1) to be positive symmetric: that is both $\hat{E}(\rho)$ and $\hat{A}(\rho)$ are symmetric matrix at all values of ρ , and $\hat{E}(\rho)$ is a positive-definite matrix at all values of ρ . To see why this would be helpful, note that if \hat{E} is positive definite then we can take its square root, $\hat{E} = CC$, for some invertible matrix C . Defining a new system vector $V = CU$, Eq. (C1) can be rewritten as

$$\dot{V} + C^{-1}\hat{A}C^{-1}V' + \dots = 0, \quad (\text{C3})$$

where the matrix $C^{-1}\hat{A}C^{-1}$ is symmetric [79]. System (C3) is clearly symmetric hyperbolic by the usual definition, and so the standard well-posedness results hold for V . Due the boundedness of C and C^{-1} , the original system (C1) is also well-posed.

Since App. B shows that \hat{E} and \hat{A} are symmetric, we only need to show that \hat{E} is positive definite. While we have been unable to prove \hat{E} is positive definite in the most general setting, we have numerically checked a handful of cases and conjecture this to be true in general. We have been able to prove it for one important special case.

We consider the special case: when $a = 0$ (scalar waves on Schwarzschild with hyperboloidal layers) the matrix \hat{E} is positive definite. Recall that \hat{E} is positive definite if $z^T \hat{E} z > 0$ for all non-trivial vectors z . When $a = 0$ this implies $f = 0$, and the matrix $E_{\pi\pi} = \mathbf{I}$ vastly simplifies. In this case its straightforward to directly check the positive-definite condition. Mimicking the block structure of \hat{E} , let $z = [a_1, a_2, \dots, a_n, b_1, b_2, \dots, b_n]$, such that a_i and b_i correspond, respectively, to the π and ϕ portions of U . Direct computation gives

$$z^T \hat{E} z = \sum_{i=1}^n a_i^2 + b_i^2 - 2Ha_i b_i.$$

Noting that $0 \leq H \leq 1$, we have two cases to consider for each i^{th} term. First suppose $a_i b_i < 0$, then clearly $a_i^2 + b_i^2 - 2Ha_i b_i \geq 0$. Next consider $a_i b_i > 0$, in which case we have

$$a_i^2 + b_i^2 - 2Ha_i b_i \geq a_i^2 + b_i^2 - 2a_i b_i \geq 0$$

where we've used Young's inequality, $ab \leq a^2/2 + b^2/2$. Such bounds can be applied to all terms in the sum, and so we have $z^T \hat{E} z \geq 0$. As an immediate consequence, upon setting $M = 0$ we deduce that the ordinary flatspace wave equation in hyperboloidal coordinates (44) also constitutes a well-posed IBVP.

Appendix D: An alternative first-order reduction

Throughout the main body of this paper, we have worked with a first-order reduction of Eq. (9) that arise from the reduction variables $\pi_{\ell m} = -\frac{\partial \psi_{\ell m}}{\partial t}$ and $\phi_{\ell m} = \frac{\partial \psi_{\ell m}}{\partial r_*}$ followed by a coordination transformation 18. Appendix C shows the resulting system to be symmetric hyperbolic when $a = 0$.

Different choices in our first-order reduction can lead to different systems with different hyperbolicity classifications. In this appendix we consider a reasonable set of choices that leads to a strictly hyperbolic system by not symmetric hyperbolic. Through numerical experiments, and as documented in Sec. IV, we found this formulation to be problematic leading to a loss of convergence. While we lack a full understanding of the issue, we note that symmetric hyperbolic systems are automatically well-posed IBVPs and often have nice numerical properties after discretization. On the other hand, strictly hyperbolic systems need not be well-posed when one of the wave speeds is 0 on the boundary [76, 77]. We note that at the rightmost boundary, $\rho = s$, one of the system's wavespeeds is 0. However, we caution the reader that because we do not understand the observed problematic behavior, we cannot entirely rule out more pedestrian explanations like a code bug. However, we did spend significant effort checking the correctness of our code and carefully considered issues such as catastrophic cancellation that might lead to loss of accuracy near $\rho = s$.

Using the hyperboloidal layer approach described in Sec. IID, the 1+1 scalar wave Eq. (9) becomes

$$\begin{aligned} & - (1 - H^2) \ddot{\psi}_{\ell m} + (1 - H)^2 \psi''_{\ell m} + \frac{\Delta a^2}{(r^2 + a^2)^2} c_{Lm}^\ell \ddot{\psi}_{Lm} \\ & - 2H(1 - H) \dot{\psi}'_{\ell m} - H'(1 - H) \dot{\psi}_{\ell m} - H'(1 - H) \psi'_{\ell m} \\ & - \frac{4imMar}{(r^2 + a^2)^2} \dot{\psi}_{\ell m} + V_{\ell m}(r) \psi_{\ell m} = g_{\ell m}(t, r), \end{aligned} \quad (\text{D1})$$

where we use an over-dot to denote ∂/∂_τ differentiation, a prime for differentiation by ∂/∂_ρ , and the various other quantities appearing in this equation have been defined in Sec. IID. To the left of the layer, where $\rho < R$, we have $H = 0$ and so both Eq. (9) and Eq. (D1) are identical. The coefficients of each term in Eq. (D1) are finite at $\rho = s$, which can be seen by noting that as $\rho \rightarrow s$ we have $(1 - H) \sim \Omega^2 \sim r_*^{-2} \sim r^{-2}$ [19, 56].

To carry out a first-order reduction, we introduce two

new variables,

$$\pi_{\ell m} = -\frac{\partial\psi_{\ell m}}{\partial\tau}, \quad \phi_{\ell m} = \frac{\partial\psi_{\ell m}}{\partial\rho}. \quad (\text{D2})$$

The following first-order system corresponds to the original second-order wave equation (D1):

$$\dot{\psi}_{\ell m} = -\pi_{\ell m} \quad (\text{D3a})$$

$$(1-H^2)\dot{\pi}_{\ell m} - \frac{\Delta a^2}{(r^2+a^2)^2}c_{Lm}^\ell\dot{\pi}_{Lm} - H(1-H)\dot{\phi}_{\ell m} = -(1-H)^2\phi'_{\ell m} - H(1-H)\pi'_{\ell m} \\ - H'(1-H)\pi_{\ell m} - \frac{4imMar}{(r^2+a^2)^2}\pi_{\ell m} + H'(1-H)\phi_{\ell m} - V_{\ell m}(r)\psi_{\ell m} + g_{\ell m}(t,r) \quad (\text{D3b})$$

$$\dot{\phi}_{\ell m} = -\partial_\rho\pi_{\ell m}. \quad (\text{D3c})$$

where in carrying out the first-order reduction, we replaced the mixed-partial derivative term as $2\dot{\psi}'_{\ell m} = -\partial_\rho\pi_{\ell m} + \partial_\tau\phi_{\ell m}$ and did not consider alternative choices. For example, the choice $2\dot{\psi}'_{\ell m} = -2\partial_\rho\pi_{\ell m}$ will lead to a simpler A matrix (cf. 25) but was not considered in our first-order reduction. If $\psi_{\ell m}$ solves the first-order system (D3) it also solves the original second-order equation (D1) provided $\phi_{\ell m} = \partial_\rho\psi_{\ell m}$.

Let us now put Eq. (D3) into matrix form (25). For concreteness, consider the even ℓ -mode sector with $m=0$ and $\ell_{\max}=2$. Then we have $U = [\pi_{00}, \pi_{20}, \phi_{00}, \phi_{20}]^T$, and

$$E = \begin{bmatrix} 1-H^2-fc_{00}^0 & -fc_{20}^0 & -\omega H & 0 \\ -fc_{00}^2 & 1-H^2-fc_{20}^2 & 0 & -\omega H \\ 0 & 0 & 1 & 0 \\ 0 & 0 & 0 & 1 \end{bmatrix} \quad (\text{D4})$$

and

$$\hat{A} = \begin{bmatrix} \omega H & 0 & \omega^2 & 0 \\ 0 & \omega H & 0 & \omega^2 \\ 1 & 0 & 0 & 0 \\ 0 & 1 & 0 & 0 \end{bmatrix} \quad (\text{D5})$$

with

$$\hat{B} = \begin{bmatrix} \omega H' + \mu & 0 & \omega\omega' & 0 \\ 0 & \omega H' + \mu & 0 & \omega\omega' \\ 0 & 0 & 0 & 0 \\ 0 & 0 & 0 & 0 \end{bmatrix} \quad (\text{D6})$$

and,

$$\hat{V} = [V_0\psi_0, V_2\psi_2, 0, 0]^T. \quad (\text{D7})$$

where μ and f have been defined in Eq. (17).

We immediately see that this system is not symmetric hyperbolic because \hat{A} is not symmetric, nor is $E^{-1}\hat{A}$ symmetric. However, one can show strict hyperbolicity and, noting that one of the wavespeeds is zero at $\rho=s$ (the right-most boundary), we see that \hat{A} is not invertible. Numerically, we have been unable to achieve good results with this system. For example, in the very simple case of $M=0$ (ie flatspace) the numerical solution to this system stops converging after about 4 to 5 digits of accuracy. This is shown most clearly in Fig. 3: compare ‘‘System 2’’ (the problematic one using reduction variables (D2)) and ‘‘System 1’’ (the first-order system that arise from the reduction variables (15)).

[1] Tullio Regge and John A. Wheeler, ‘‘Stability of a Schwarzschild singularity,’’ *Phys. Rev.* **108**, 1063–1069 (1957).

[2] Frank J. Zerilli, ‘‘Effective potential for even parity Regge-Wheeler gravitational perturbation equations,’’ *Phys. Rev. Lett.* **24**, 737–738 (1970).

- [3] Vincent Moncrief, “Gravitational perturbations of spherically symmetric systems. I. The exterior problem,” *Annals of Physics* **88**, 323 – 342 (1974).
- [4] Saul A. Teukolsky, “Perturbations of a Rotating Black Hole. I. Fundamental Equations for Gravitational, Electromagnetic, and Neutrino-Field Perturbations,” *Astrophysical Journal* **185**, 635–648 (1973).
- [5] Pau Amaro-Seoane *et al.*, “Laser Interferometer Space Antenna,” arXiv e-prints , arXiv:1702.00786 (2017), arXiv:1702.00786 [astro-ph.IM].
- [6] Pau Amaro-Seoane, Jonathan R Gair, Marc Freitag, M Coleman Miller, Ilya Mandel, Curt J Cutler, and Stanislav Babak, “Intermediate and extreme mass-ratio inspirals—astrophysics, science applications and detection using lisa,” *Classical and Quantum Gravity* **24**, R113 (2007).
- [7] Pau Amaro-Seoane, Bernard Schutz, and Carlos F. Sopuerta, “Gravitational Waves Notes, Issue #4 : “A Roadmap to Fundamental Physics from LISA EMRI Observations”,” arXiv e-prints , arXiv:1009.1402 (2010), arXiv:1009.1402 [astro-ph.CO].
- [8] Ryuichi Fujita and Hideyuki Tagoshi, “New numerical methods to evaluate homogeneous solutions of the teukolsky equation. ii: —solutions of the continued fraction equation—,” *Progress of theoretical physics* **113**, 1165–1182 (2005).
- [9] Lee Samuel Finn and Kip S Thorne, “Gravitational waves from a compact star in a circular, inspiral orbit, in the equatorial plane of a massive, spinning black hole, as observed by lisa,” *Physical Review D* **62**, 124021 (2000).
- [10] Kostas Glampedakis, Scott A Hughes, and Daniel Kennefick, “Approximating the inspiral of test bodies into kerr black holes,” *Physical Review D* **66**, 064005 (2002).
- [11] Steve Drasco and Scott A Hughes, “Gravitational wave snapshots of generic extreme mass ratio inspirals,” *Physical Review D* **73**, 024027 (2006).
- [12] Rodrigo Panosso Macedo, Benjamin Leather, Niels Warburton, Barry Wardell, and Anil Zenginoğlu, “Hyperboloidal method for frequency-domain self-force calculations,” *Physical Review D* **105**, 104033 (2022).
- [13] Ramon Lopez-Aleman, Gaurav Khanna, and Jorge Pullin, “Perturbative evolution of particle orbits around kerr black holes: time-domain calculation,” *Classical and Quantum Gravity* **20**, 3259 (2003).
- [14] Gaurav Khanna, “Teukolsky evolution of particle orbits around kerr black holes in the time domain: Elliptic and inclined orbits,” *Physical Review D* **69**, 024016 (2004).
- [15] Lior M Burko and Gaurav Khanna, “Accurate time-domain gravitational waveforms for extreme-mass-ratio binaries,” *Europhysics Letters* **78**, 60005 (2007).
- [16] Pranesh A Sundararajan, Gaurav Khanna, and Scott A Hughes, “Towards adiabatic waveforms for inspiral into kerr black holes: A new model of the source for the time domain perturbation equation,” *Physical Review D* **76**, 104005 (2007).
- [17] Pranesh A Sundararajan, Gaurav Khanna, Scott A Hughes, and Steve Drasco, “Towards adiabatic waveforms for inspiral into kerr black holes. ii. dynamical sources and generic orbits,” *Physical Review D* **78**, 024022 (2008).
- [18] Pranesh A Sundararajan, Gaurav Khanna, and Scott A Hughes, “Binary black hole merger gravitational waves and recoil in the large mass ratio limit,” *Physical Review D* **81**, 104009 (2010).
- [19] Anil Zenginoğlu and Gaurav Khanna, “Null infinity waveforms from extreme-mass-ratio inspirals in kerr spacetime,” *Physical Review X* **1**, 021017 (2011).
- [20] Lior M Burko and Gaurav Khanna, “Gravitational waves from a plunge into a nearly extremal kerr black hole,” *Physical Review D* **94**, 084049 (2016).
- [21] Scott E Field, Sigal Gottlieb, Zachary J Grant, Leah F Isherwood, and Gaurav Khanna, “A gpu-accelerated mixed-precision weno method for extremal black hole and gravitational wave physics computations,” *Communications on Applied Mathematics and Computation* **5**, 97–115 (2023).
- [22] Scott E Field, Sigal Gottlieb, Gaurav Khanna, and Ed McClain, “Discontinuous galerkin method for linear wave equations involving derivatives of the dirac delta distribution,” arXiv preprint arXiv:2211.14390 (2022).
- [23] Carlos F Sopuerta and Pablo Laguna, “Finite element computation of the gravitational radiation emitted by a pointlike object orbiting a nonrotating black hole,” *Physical Review D* **73**, 044028 (2006).
- [24] Istvan Racz and Gábor Zs Tóth, “Numerical investigation of the late-time kerr tails,” *Classical and Quantum Gravity* **28**, 195003 (2011).
- [25] Enno Harms, Sebastiano Bernuzzi, and Bernd Brügmann, “Numerical solution of the 2+ 1 teukolsky equation on a hyperboloidal and horizon penetrating foliation of kerr and application to late-time decays,” *Classical and Quantum Gravity* **30**, 115013 (2013).
- [26] Károly Csukás, István Rácz, and Gábor Zsolt Tóth, “Numerical investigation of the dynamics of linear spin $s = \pm 1, \pm 2$ fields,” *Physical Review D* **100**, 104025 (2019).
- [27] William Krivan, Pablo Laguna, Philippos Papadopoulos, and Nils Andersson, “Dynamics of perturbations of rotating black holes,” *Physical Review D* **56**, 3395 (1997).
- [28] Enno Harms, Sebastiano Bernuzzi, Alessandro Nagar, and Anil Zenginoğlu, “A new gravitational wave generation algorithm for particle perturbations of the kerr spacetime,” *Classical and Quantum Gravity* **31**, 245004 (2014).
- [29] Stefanos Aretakis, “A note on instabilities of extremal black holes under scalar perturbations from afar,” *Classical and Quantum Gravity* **30**, 095010 (2013).
- [30] Y. Angelopoulos, Stefanos Aretakis, and Dejan Gajic, “Horizon hair of extremal black holes and measurements at null infinity,” *Phys. Rev. Lett.* **121**, 131102 (2018), arXiv:1809.10037 [gr-qc].
- [31] Lior M. Burko, Gaurav Khanna, and Subir Sabharwal, “(Transient) Scalar Hair for (Nearly) Extreme Black Holes,” *Phys. Rev. Research.* **1**, 033106 (2019), arXiv:1906.03116 [gr-qc].
- [32] Björn Engquist, Anna-Karin Tornberg, and Richard Tsai, “Discretization of dirac delta functions in level set methods,” *Journal of Computational Physics* **207**, 28–51 (2005).
- [33] Anna-Karin Tornberg and Björn Engquist, “Numerical approximations of singular source terms in differential equations,” *Journal of Computational Physics* **200**, 462–488 (2004).
- [34] Jonathan Thornburg and Barry Wardell, “Scalar self-force for highly eccentric equatorial orbits in kerr spacetime,” *Physical Review D* **95**, 084043 (2017).
- [35] Peter Diener, Ian Vega, Barry Wardell, and Steven Dettweiler, “Self-consistent orbital evolution of a particle around a schwarzschild black hole,” *Physical Review Let-*

- ters **108**, 191102 (2012).
- [36] Niels Warburton and Barry Wardell, “Applying the effective-source approach to frequency-domain self-force calculations,” *Physical Review D* **89**, 044046 (2014).
- [37] Priscilla Canizares, Carlos F Sopena, and José Luis Jaramillo, “Pseudospectral collocation methods for the computation of the self-force on a charged particle: Generic orbits around a schwarzschild black hole,” *Physical Review D* **82**, 044023 (2010).
- [38] Priscilla Canizares and Carlos F Sopena, “Simulations of extreme-mass-ratio inspirals using pseudospectral methods,” in *Journal of Physics: Conference Series*, Vol. 154 (IOP Publishing, 2009) p. 012053.
- [39] Scott E Field, Jan S Hesthaven, and Stephen R Lau, “Discontinuous galerkin method for computing gravitational waveforms from extreme mass ratio binaries,” *Classical and Quantum Gravity* **26**, 165010 (2009).
- [40] Dario Nunez, Juan Carlos Degollado, and Carlos Palenzuela, “One dimensional description of the gravitational perturbation in a kerr background,” *Physical Review D* **81**, 064011 (2010).
- [41] Leo Stein, *Probes of strong-field gravity*, Ph.D. thesis, Massachusetts Institute of Technology (2012).
- [42] Sam R Dolan, “Superradiant instabilities of rotating black holes in the time domain,” *Physical Review D* **87**, 124026 (2013).
- [43] Leor Barack and Paco Giudice, “Time-domain metric reconstruction for self-force applications,” *Physical Review D* **95**, 104033 (2017).
- [44] Charalampos Markakis, Sean Bray, and Anil Zenginoğlu, “Symmetric integration of the 1+1 teukolsky equation on hyperboloidal foliations of kerr spacetimes,” arXiv preprint arXiv:2303.08153 (2023).
- [45] William H Reed and Thomas R Hill, *Triangular mesh methods for the neutron transport equation*, Tech. Rep. (Los Alamos Scientific Lab., N. Mex.(USA), 1973).
- [46] J.S. Hesthaven and T. Warburton, *Nodal Discontinuous Galerkin Methods: Algorithms, Analysis, and Applications* (Springer, Berlin, New York, 2008).
- [47] Bernardo Cockburn, George E Karniadakis, and Chi-Wang Shu, *The development of discontinuous Galerkin methods* (Springer, 2000).
- [48] Bernardo Cockburn, “Devising discontinuous galerkin methods for non-linear hyperbolic conservation laws,” *Journal of Computational and Applied Mathematics* **128**, 187–204 (2001).
- [49] Bernardo Cockburn and Chi-Wang Shu, “The runge-kutta discontinuous galerkin method for conservation laws v: multidimensional systems,” *Journal of computational physics* **141**, 199–224 (1998).
- [50] Kai Fan, Wei Cai, and Xia Ji, “A generalized discontinuous galerkin (gdg) method for schrödinger equations with nonsmooth solutions,” *Journal of Computational Physics* **227**, 2387–2410 (2008).
- [51] K. S. Thorne, “Multipole Expansions of Gravitational Radiation,” *Rev. Mod. Phys.* **52**, 299–339 (1980).
- [52] W. N. Bailey, “On the product of two legendre polynomials,” *Mathematical Proceedings of the Cambridge Philosophical Society* **29**, 173–177 (1933).
- [53] James M Bardeen, William H Press, and Saul A Teukolsky, “Rotating black holes: locally nonrotating frames, energy extraction, and scalar synchrotron radiation,” *The Astrophysical Journal* **178**, 347–370 (1972).
- [54] Niels Warburton and Leor Barack, “Self-force on a scalar charge in kerr spacetime: Circular equatorial orbits,” *Physical Review D* **81**, 084039 (2010).
- [55] Scott A Hughes, “Evolution of circular, nonequatorial orbits of kerr black holes due to gravitational-wave emission,” *Physical Review D* **61**, 084004 (2000).
- [56] Anil Zenginoğlu, “Hyperboloidal layers for hyperbolic equations on unbounded domains,” *Journal of Computational Physics* **230**, 2286–2302 (2011).
- [57] Sebastiano Bernuzzi, Alessandro Nagar, and Anil Zenginoğlu, “Binary black hole coalescence in the large-mass-ratio limit: the hyperboloidal layer method and waveforms at null infinity,” *Physical Review D* **84**, 084026 (2011).
- [58] William Krivan, Pablo Laguna, and Philippos Papadopoulos, “Dynamics of scalar fields in the background of rotating black holes,” *Physical Review D* **54**, 4728 (1996).
- [59] William Krivan, Pablo Laguna, Philippos Papadopoulos, and Nils Andersson, “Dynamics of perturbations of rotating black holes,” *Phys. Rev. D* **56**, 3395–3404 (1997).
- [60] Scott E Field and Stephen R Lau, “Fast evaluation of far-field signals for time-domain wave propagation,” *Journal of Scientific Computing* **64**, 647–669 (2015).
- [61] Lawrence E Kidder, Scott E Field, Francois Foucart, Erik Schnetter, Saul A Teukolsky, Andy Bohn, Nils Deppe, Peter Diener, François Hébert, Jonas Lippuner, *et al.*, “Spectre: a task-based discontinuous galerkin code for relativistic astrophysics,” *Journal of Computational Physics* **335**, 84–114 (2017).
- [62] Slimane Adjerid and Mahboub Baccouch, “The discontinuous galerkin method for two-dimensional hyperbolic problems. part i: Superconvergence error analysis,” *Journal of Scientific Computing* **33**, 75–113 (2007).
- [63] Waixiang Cao and Zhimin Zhang, “Superconvergence of local discontinuous galerkin methods for one-dimensional linear parabolic equations,” *Mathematics of Computation* **85**, 63–84 (2016).
- [64] Liangyue Ji, Paulien Van Slingerland, Jennifer K Ryan, and Kees Vuik, “Superconvergent error estimates for position-dependent smoothness-increasing accuracy-conserving (siac) post-processing of discontinuous galerkin solutions,” *Mathematics of computation* , 2239–2262 (2014).
- [65] Richard H Price, “Nonspherical perturbations of relativistic gravitational collapse. i. scalar and gravitational perturbations,” *Physical Review D* **5**, 2419 (1972).
- [66] Shahar Hod, “Mode-coupling in rotating gravitational collapse of a scalar field,” *Physical Review D* **61**, 024033 (1999).
- [67] Reinaldo Gleiser, Richard Price, and Jorge Pullin, “Late-time tails in the kerr spacetime,” *Classical and Quantum Gravity* **25**, 072001 (2008).
- [68] Manuel Tiglio, Lawrence Kidder, and Saul Teukolsky, “High accuracy simulations of kerr tails: coordinate dependence and higher multipoles,” *Classical and Quantum Gravity* **25**, 105022 (2008).
- [69] Lior Burko and Gaurav Khanna, “Late-time kerr tails revisited,” *Classical and Quantum Gravity* **26**, 015014 (2008).
- [70] Lior M Burko and Gaurav Khanna, “Late-time kerr tails: generic and non-generic initial data sets, up modes, and superposition,” *Classical and Quantum Gravity* **28**, 025012 (2011).
- [71] Anil Zenginoğlu, Gaurav Khanna, and Lior Burko, “Intermediate behavior of kerr tails,” *Gen Relativ Gravit* **46**,

- 1672 (2014).
- [72] Lior M Burko and Gaurav Khanna, “Mode coupling mechanism for late-time kerr tails,” *Physical Review D* **89**, 044037 (2014).
- [73] Scott E Field, Jan S Hesthaven, and Stephen R Lau, “Persistent junk solutions in time-domain modeling of extreme mass ratio binaries,” *Physical Review D* **81**, 124030 (2010).
- [74] “Black Hole Perturbation Toolkit,” (bhptoolkit.org).
- [75] Barry Wardell, Niels Warburton, Leanne Durkan, Kevin Cunningham, Benjamin Leather, znasipak, and TheoTorresV, “[BlackHolePerturbationToolkit/Teukolsky: Teukolsky 0.3.0](https://doi.org/10.5281/zenodo.7037857),” [10.5281/zenodo.7037857](https://doi.org/10.5281/zenodo.7037857) (2022).
- [76] Olivier Sarbach and Manuel Tiglio, “Continuum and discrete initial-boundary value problems and einstein’s field equations,” *Living reviews in relativity* **15**, 1–194 (2012).
- [77] Andrew Majda and Stanley Osher, “Initial-boundary value problems for hyperbolic equations with uniformly characteristic boundary,” *Communications on Pure and Applied Mathematics* **28**, 607–675 (1975).
- [78] Bertil Gustafsson, Heinz-Otto Kreiss, and Joseph Olinger, *Time dependent problems and difference methods*, Vol. 24 (John Wiley & Sons, 1995).
- [79] R Courant and D Hilbert, “Methods of mathematical physics (interscience publ., new york and london), vol. 1,” vol **2**, 830 (1962).